Wind Loading on CSP Collectors

Shashank Yellapantula

National Renewable Energy Laboratory

NREL is a national laboratory of the U.S. Department of Energy
Office of Energy Efficiency & Renewable Energy
Operated by the Alliance for Sustainable Energy, LLC

This report is available at no cost from the National Renewable Energy Laboratory (NREL) at www.nrel.gov/publications.

Contract No. DE-AC36-08GO28308

Technical Report
NREL/TP- 2C00-92445
December 2024

Wind Loading on CSP Collectors

Shashank Yellapantula

National Renewable Energy Laboratory

Suggested Citation
Yellapantula, Shashank. 2024. *Wind Loading on CSP Collectors*. Golden, CO: National Renewable Energy Laboratory. NREL/TP-2C00-92445 https://www.nrel.gov/docs/fy25osti/92445.pdf.

NREL is a national laboratory of the U.S. Department of Energy
Office of Energy Efficiency & Renewable Energy
Operated by the Alliance for Sustainable Energy, LLC

This report is available at no cost from the National Renewable Energy Laboratory (NREL) at www.nrel.gov/publications.

Contract No. DE-AC36-08GO28308

Technical Report
NREL/TP- 2C00-92445
December 2024

National Renewable Energy Laboratory
15013 Denver West Parkway
Golden, CO 80401
303-275-3000 • www.nrel.gov

NOTICE

This work was authored by the National Renewable Energy Laboratory, operated by Alliance for Sustainable Energy, LLC, for the U.S. Department of Energy (DOE) under Contract No. DE-AC36-08GO28308. Funding provided by the U.S. Department of Energy Office of Energy Efficiency and Renewable Energy Solar Energy Technologies Office. The views expressed herein do not necessarily represent the views of the DOE or the U.S. Government.

Final Technical Report (FTR)

Cover Page

a. *Federal Agency*	Department of Energy	
b. *Award Number*	DE-EE0038483	
c. *Project Title*	Wind loading on CSP collectors	
d. *Recipient Organization*	National Renewable Energy Laboratory (NREL)	
e. *Project Period*	*Start:* 10/1/2021	*End:* 9/30/2024
f. *Principal Investigator (PI)*	Name: Shashank Yellapantula Title: Senior Scientist Email address: shashank.yellapantula@nrel.gov Phone number: 303-264-8595	
g. *Business Contact (BC)*	Name: Craig Turchi Title: CSP Program Lead Email address: craig.turchi@nrel.gov Phone number: 303-384-7565	
h. *Certifying Official (if different from the PI or BC)*	Name Title Email address Phone number	

Signature of Certifying Official *12/9/2024* *Date*

By signing this report, I certify to the best of my knowledge and belief that the report is true, complete, and accurate. I am aware that any false, fictitious, or fraudulent information, misrepresentations, half-truths, or the omission of any material fact, may subject me to criminal, civil or administrative penalties for fraud, false statements, false claims or otherwise. (U.S. Code Title 18, Section 1001, Section 287 and Title 31, Sections 3729-3730). I further understand and agree that the information contained in this report are material to Federal agency's funding decisions and I have any ongoing responsibility to promptly update the report within the time frames stated in the terms and conditions of the above referenced Award, to ensure that my responses remain accurate and complete.

Acknowledgement

This material is based upon work supported by the U.S. Department of Energy's Office of Energy Efficiency and Renewable Energy (EERE) Solar Energy Technologies Office (SETO) under the Award Number DE-EE0038483.

Disclaimer

Executive Summary

The project significantly enhanced the community's understanding of the fundamental physics drivers underlying the wind-loading experienced by concentrating solar power (CSP) collector structures (i.e., parabolic troughs and heliostats) as well as their support structures. This project had two overarching objectives: (1) detailed measurements to characterize the prevailing wind conditions and resulting operational loads on collector structures, and (2) development and validation of a computationally efficient, high-fidelity modeling tool capable of predicting wind-loading in deep-array installations. Over three years, we conducted comprehensive at-scale field measurements of the atmospheric turbulent wind conditions, and the resulting wind loads on parabolic troughs and heliostats. Two at-scale measurement campaigns yielded first-of-its-kind, high-resolution, long-term datasets that are used to characterize the complex flow field and wind loading on parabolic-troughs and heliostats in operational power plants. The high-resolution measurements collected during these campaigns were used to validate the high-fidelity computational models developed at NREL. These open-source computationally efficient models were shown to be accurate in predicting wind-driven loads on collectors without the need for a large supercomputer.

Table of Contents

1 Background

Previous research on parabolic troughs and heliostats [1, 2] has provided valuable insights into the dynamics of wind loading. For heliostats, wind tunnel studies [3] and full-scale measurements [4] agree that wind loads are highest at the edge of a collector field and tend to level off after the first few rows. Wind tunnel tests [5] showed that wind design loads depend on heliostat size and terrain roughness. The importance of dynamic loading on heliostats due to turbulence was pointed out [6], especially in the inner field [7], as were effects on optical efficiency and fatigue loading [8]. For parabolic troughs, it was also observed that static wind loads decrease after the first row [1, 9, 10] and level out behind [9, 11], but dynamic loads are increased after the first row [12]. Further, the dependence of wind loads on trough angles was also highlighted in previous studies [13, 14, 11]. Additional studies focused on wind-driven structural deflections [19] leading to spillage and decreased optical performance [18]. Several other studies have shown that the wind-facing first row of collectors produces a flow pattern that induces dynamic loads on the second row [15, 12, 17, 16].

Most of this existing knowledge is based on idealized settings, such as small test collector fields or wind tunnel models. In a realistic power plant setting, the solar collectors track the sun throughout the day, leading to complex interactions with the wind with a distinct diurnal and seasonal cycle. Although wind tunnel tests are a well-established method for estimating static wind loads, challenges persist in reproducing the entire turbulence spectrum leading to critical knowledge gaps in understanding dynamic wind loading. Further, there are no universal design guidelines for dynamic wind loading on CSP solar collectors. The unique geometry and operation principle of CSP collectors complicates the application of general civil engineering standards, such as ASCE-7 [20].

2 Project Objectives

This project completed two complementary activities: (1) an at-scale field measurement campaign in an operational collector field, and (2) a computational fluid dynamic (CFD)-based CSP collector wind-loading analysis toolset. The at-scale field measurement campaign generated a first-of-a-kind, comprehensive, high-resolution wind-loading datasets that does not suffer from the scale limitations of wind-tunnel tests. Additionally, the CFD-based CSP collector field wind-loading analysis toolset leverages decades of NREL's wind-modeling expertise to accurately model the inflow conditions as a function of surface temperature and local terrain roughness, the evolution and dissipation of wakes in deep-array configurations, and the mean and unsteady loading experienced by interior collectors. The technical tasks along with the project results and the associated milestones, completed successfully on time, are described in detail in the following sections.

3 Project Results and Discussion

3.1 Wind and loads measurement in a parabolic trough power plant

The NREL team generated a unique dataset of wind and structural loads measurements in an operational parabolic trough power plant. The project team installed four meteorological towers, each with three sonic anemometers at various heights. The first tower, inflow tower, was positioned outside of the collector field to measure the undisturbed flow coming from the west of the plant. Additionally, three more meteorological towers with three sonic anemometers each were installed in the wake of the first three trough rows to measure the wind flow modification by each of the rows. Figure 1 shows the arrangement of all the towers installed at the edge and within the trough field. A scanning lidar was also installed to measure wind profiles over a large area over the trough field. Figure 2 shows the overall layout of all the wind instrumentation installed at the Nevada Solar One (NSO) parabolic trough power plant.

Figure 1: An 15-m tall inflow met tower (left), and locations of three 8-m tall met towers are shown with red circles in the right figure.

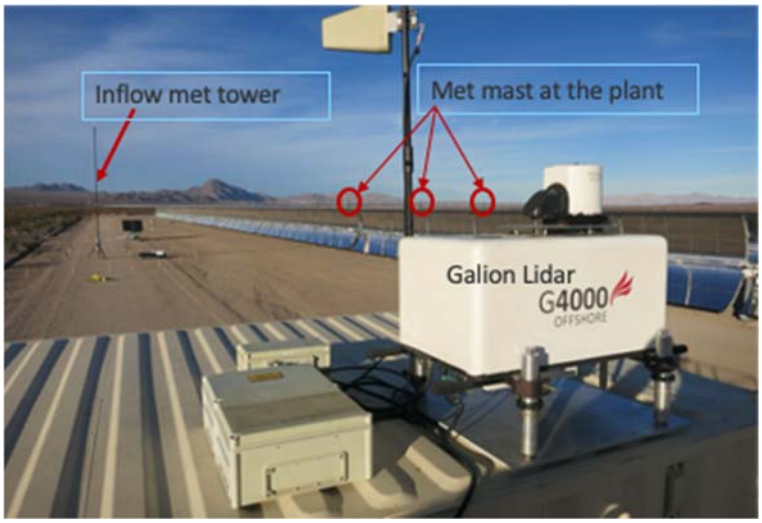

Figure 2: The overall setup of the field deployment which contains a scanning lidar on top of two stacked storage containers, a 15-m tall met tower, and three 8-m tall met towers.

The layout of the sonic anemometers on each of the met towers is shown in Figure 3. The lowest sonics measures the wind conditions at approximate hinge height.

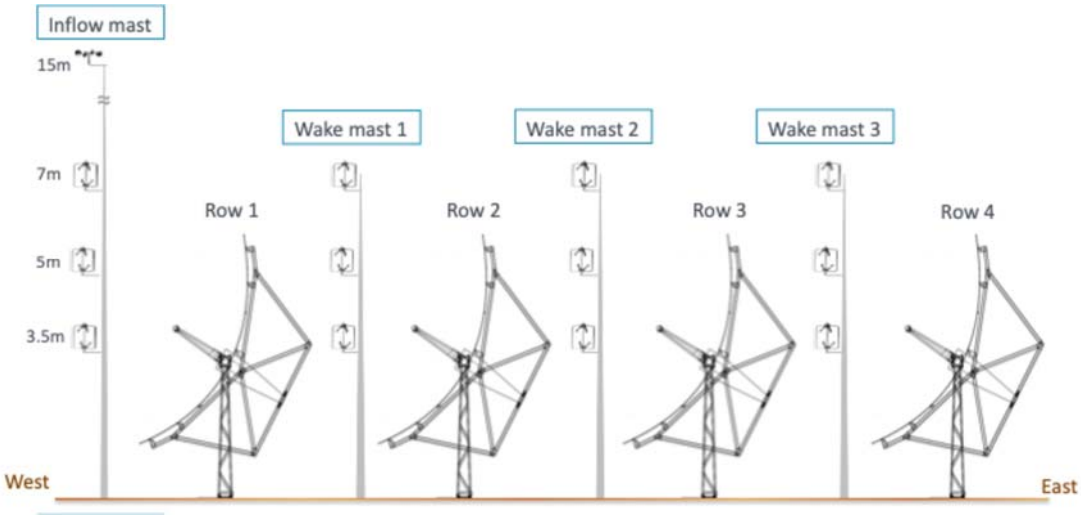

Figure 3: Sonic anemometer placement on each of the met-tower for high resolution wind measurement.

One of the major accomplishments of this project was to create a conceptual model for wind field modification by the trough rows (Figure 4). By analyzing the long-term wind profiles measured by met towers and lidar, the project team was able to explain how the undisturbed wind flow from the west is modified by the trough rows through a wind slowdown and directionality change, and breakdown of larger turbulent eddies into smaller ones.

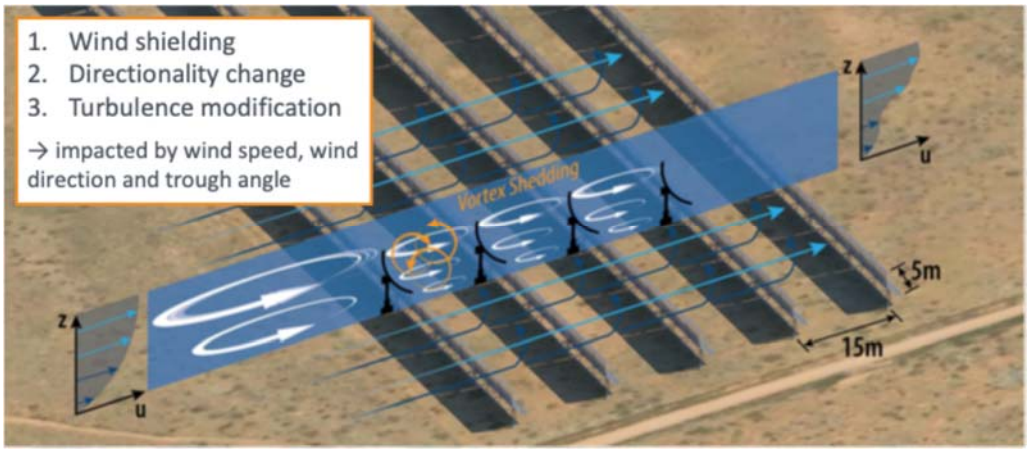

Figure 4: Model of modification of wind profile over the troughs.

Previous studies have shown that the turbulent wind field is highly impacted by the wind blowing perpendicular to the parabolic trough rows. Therefore, we focus our analysis on winds from the west which are perpendicular to the trough rows (15% of the inflow data). In the analysis that follows, we illustrate how the wind coming from the west is modified by studying the change of vertical profiles within the first four rows. Figure 5 shows that as the wind flows over the first row, the wind speed is reduced in between the subsequent rows. A less pronounced wind speed decrease is also observed above the troughs. A 35% reduction in median wind speed across row 1 is observed at 7m height above the troughs whereas the measurements at 3.5m near hinge height show a significant wind speed reduction of 60%. The lower wind speed between rows two to four remains nearly constant.

As will be discussed later, this wind-speed sheltering has a direct effect on the structural loads further into the trough field. It is well-known that a bluff body, in our case parabolic troughs, reduces the wind speed, and this knowledge is frequently applied to the design of structures within the trough field. The position in the field and the trough angle, which influences the normal area of the trough facing the flow, both impact the magnitude of the reduction in mean wind speeds. The mean drag force, normal to the troughs, decreases as a result of the reduced wind speed behind the first few rows, as will be demonstrated in the subsequent sections.

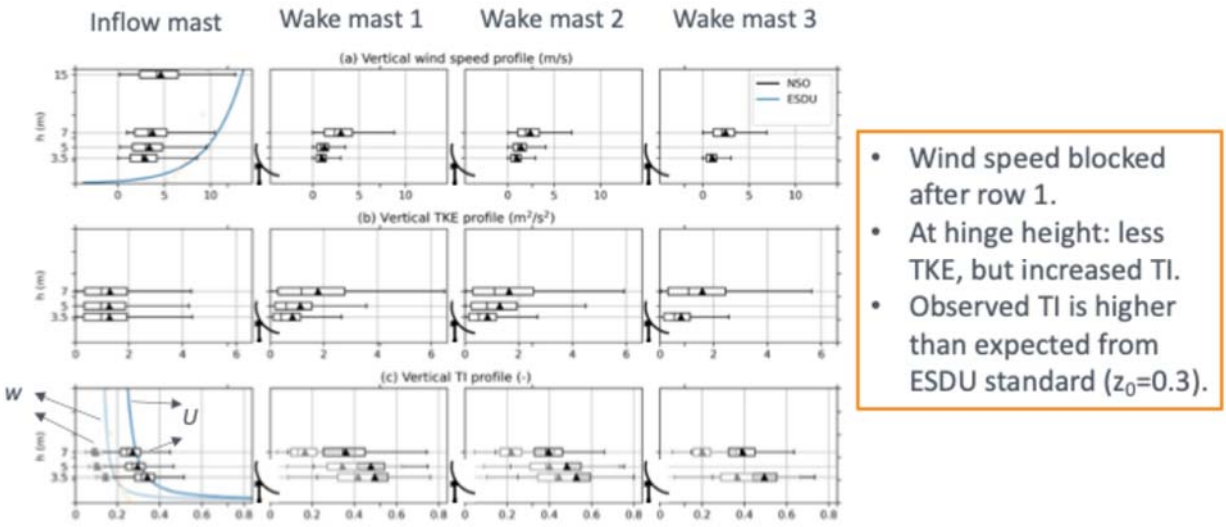

Figure 5: Vertical profiles of wind and turbulence modified by trough rows.

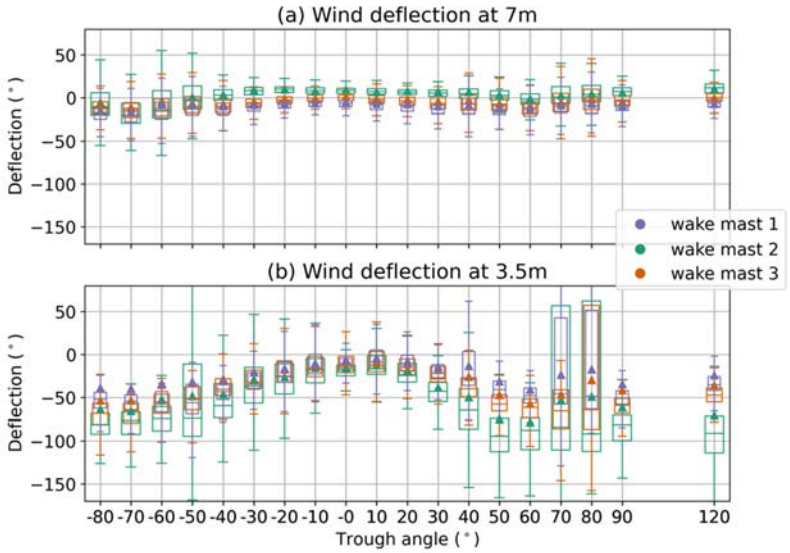

Figure 6: Deflection of wind direction depending on trough angle, measured at 3.5m height and 7m height.

Within the trough field, the wind is not only blocked but also redirected. The inflow wind direction is distributed around 250° (west-southwest) for all the sonics on the inflow tower. In the wake of the troughs, the wind direction switches to 180° (south), corresponding to an average directionality change of up to 70°. This wind veer is most pronounced after the first row. For incoming winds from the southwest, the shift is towards the south. For the winds from the northwest direction, the shift is toward the north. However, northern wind directions are rarely observed. The magnitude of the wind veer is also impacted by the trough angle (Figure 6). Near hinge height (3.5m), upward-facing troughs create about 10° wind veer to the south, whereas trough angles greater than ±60° (both east- and west-facing), including stow, create up to 90° veer at all wake masts.

At heights above the trough field and at trough angles of ± 60º, a wind veer up to 20º to the south is visible. This wind deflection by the troughs is a unique observation and has not been reported previously in studies involving solar collectors. This wind deflection will cause asymmetric structural loads on the troughs and can help explain turbulence-induced edge effects of the array as well as differences in convective losses on the absorber tubes.

The inflow approaching over the surrounding desert terrain, approaching the parabolic trough fields, can be viewed as a change in surface roughness, impacting the vertical distribution of flow properties. A review article about surface heterogeneities [21] reaffirms the findings presented here. In one study [21], the authors mention that a large and persistent secondary circulation can form when the flow approaches a roughness change not perpendicular but at an angle, as observed in our case with rows of parabolic troughs.

Further, field observations of a ridge forest [22] reveal a highly three-dimensional flow with significant directional shear at different heights, comparable to the change in wind direction we observe between trough rows. The authors note that this is not captured in idealized two-dimensional numerical studies but could subject trees and other structures to additional torsional forces. Unfortunately, due to a lack of access to certain structural members, moments and forces along the trough rotation axis were not measured in this study.

Turbulence kinetic energy (TKE) is constant across height in the incoming flow (Figure 7a). After reaching the trough field, TKE increases in the upper half and above the troughs and decreases at hinge height. The turbulence intensity (TI) relates vertical and horizontal velocity fluctuations to the mean horizontal wind speed. The inflow TI profile (Figure 7b) exhibits a typical increase closer to the ground, also present in the ESDU (a standard for boundary layer characterization, [41]) and Hosoya (our reference wind tunnel tests_[9]) cases. However, our observations at NSO reveal much higher TIs (for both horizontal and vertical wind components) compared to these other studies. This large difference in turbulence characteristics between idealized conditions and field measurements stems from the hilly terrain west of NSO, creating an upstream surface roughness substantially higher than the assumed desert value. Additionally, it has been suggested [23] that in CSP collector wind tunnel experiments, TI is often underestimated unless the surface roughness parameter z_0 is adequately increased to achieve Jensen number ($Je = W/z_0$) similarity. Above and within the troughs, TI, in both directions, increases compared to the inflow, particularly within the field, and with a more pronounced increase in vertical TI. In the wake, we observe very high TI values up to 80%, which is due to the strong blockage of the mean wind speed. Mean TI values are in the same range as observed between heliostats [24].

While turbulent length scales (Figure 7c) match the ESDU values better, ESDU underestimates the size of horizontal eddies and overestimates the vertical eddy sizes. Within the trough field, all eddy sizes are found to be reduced, indicating a breakup of larger eddies into more smaller ones. In addition to studying vertical and horizontal components separately, the ratio of vertical to horizontal TIs and length scales provides insights into anisotropy of the flow. For both TI and length scales, turbulent eddies become more isotropic in the wake between the troughs. In the inflow and above the troughs, we observe a typical value of $TI_w/TI_U \sim 0.3$. The smaller turbulent eddies are still large enough, on the order of the trough dimension, to effectively produce fluctuating loads on the troughs and can even interfere with the natural frequencies of the structures [25].

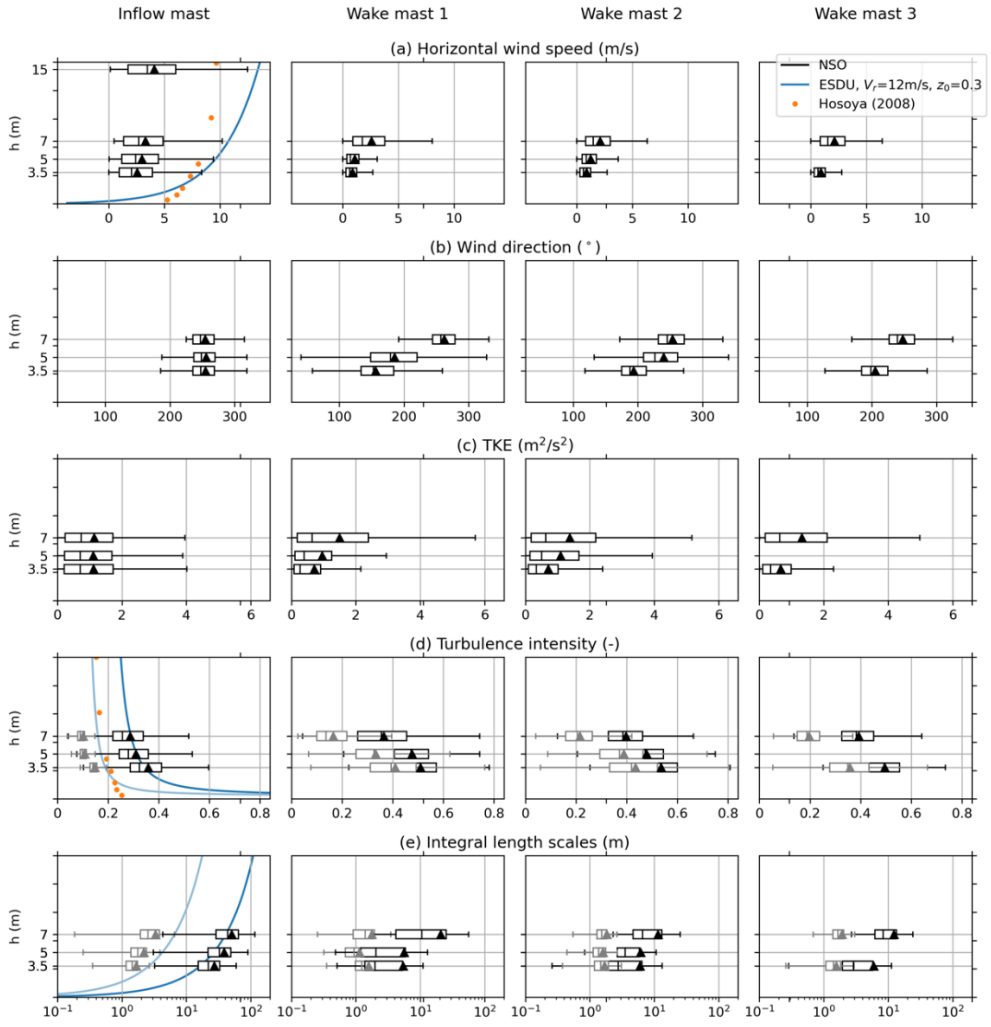

Figure 7: Vertical profiles for TKE, TI, and length scales for all 4 met-towers.

Lidar data analysis from the parabolic trough plant

Figure 8 (left image) shows the PPI (horizontal) scanning pattern deployed at the NSO parabolic trough plant. The region marked by the blue circle is the dead zone where a low signal to noise ratio is seen and therefore the data in that zone is discarded. Figure 8 (right image) shows a representative wind speed profile over the plant, captured by the scanning lidar. Wind flowing into the plant from the west will be considered for analysis in the following section.

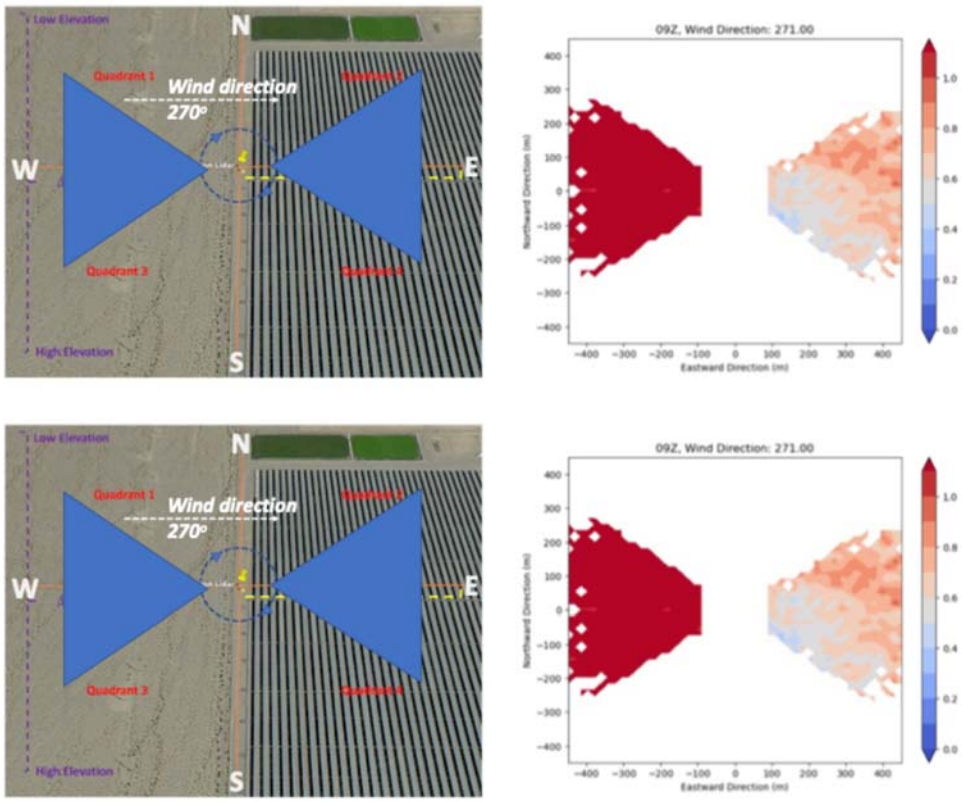

Figure 8: Schematic of the PPI Lidar scan (left) and a sample western wind speed profile over the collector field, normalized to the inflow wind speed.

Figure 9 indicates the spatial pattern of the mean normalized wind speed during nine instances of wind coming in from the west. At the edge of the plant, shielding of wind by the upstream rows reduces the mean wind speed, represented by the blue regions. However, further into the field a recovery in wind speed is observed as wind moves further into the plant and the magnitude of the recovery varies case by case depending on many factors such as turbulent intensity, atmospheric stability, and the angular position of the parabolic trough. Overall, analysis of data spread over several cases reveals that the wind speed over the trough rows could recover by 15-20%, most likely due to the momentum extraction from the air above through enhanced turbulent mixing. This recovery of wind speed over the troughs, in the interior of the plant, leads to increased wind shear on the outer edge of the parabolic troughs which would in turn lead to higher turning moments.

Figure 10 shows a schematic of the potential impact of increased wind shear on the loads experienced by parabolic troughs under western wind conditions. When the wind hits the front rows, both wind speed above and within the trough rows will reduce resulting in less shear and

less turning moments. Further into the plant, however, the wind speed above the troughs recovers due to momentum transport from enhanced turbulent mixing. Therefore, the vertical gradient of wind speed increases. This would lead to an increase in turning moments around the hinge axis which would impact the supporting structure of the parabolic troughs, particularly for the rows in the interior of the plant.

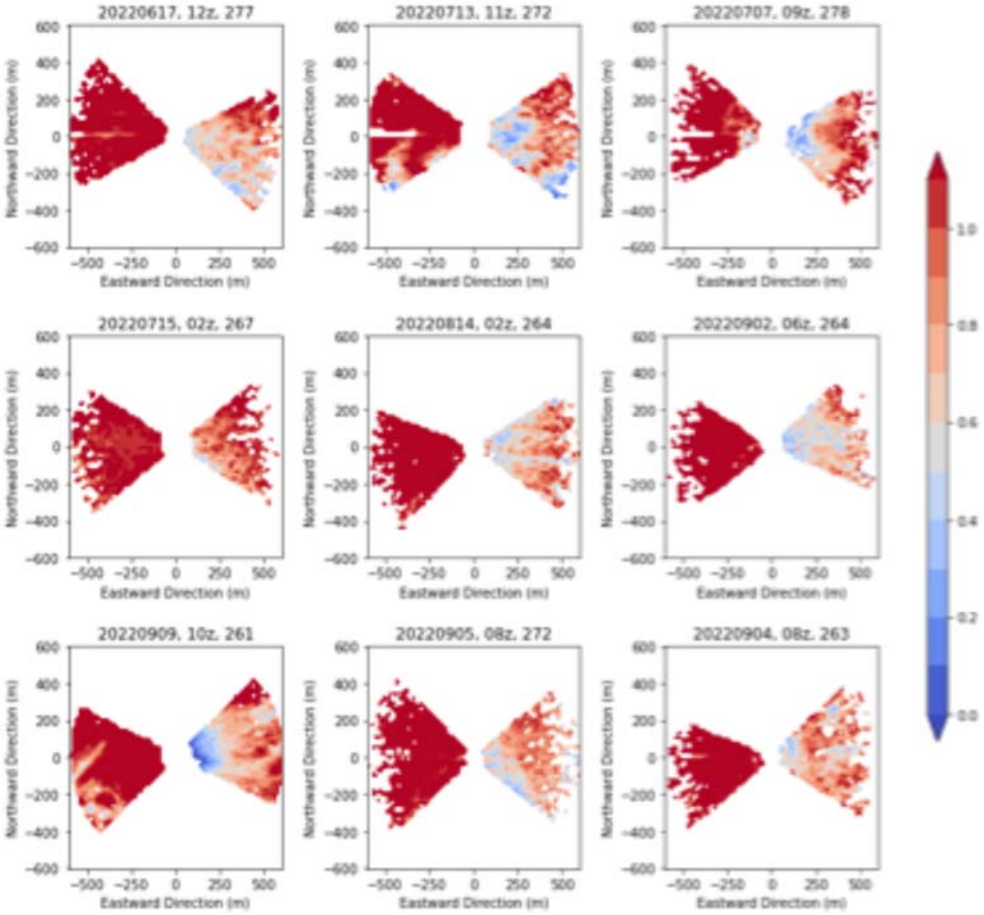

Figure 9: Composite of 9 instances of wind blowing from the west captured by the PPI lidar scan. The color represents the wind speed normalized to the mean inflow wind speed.

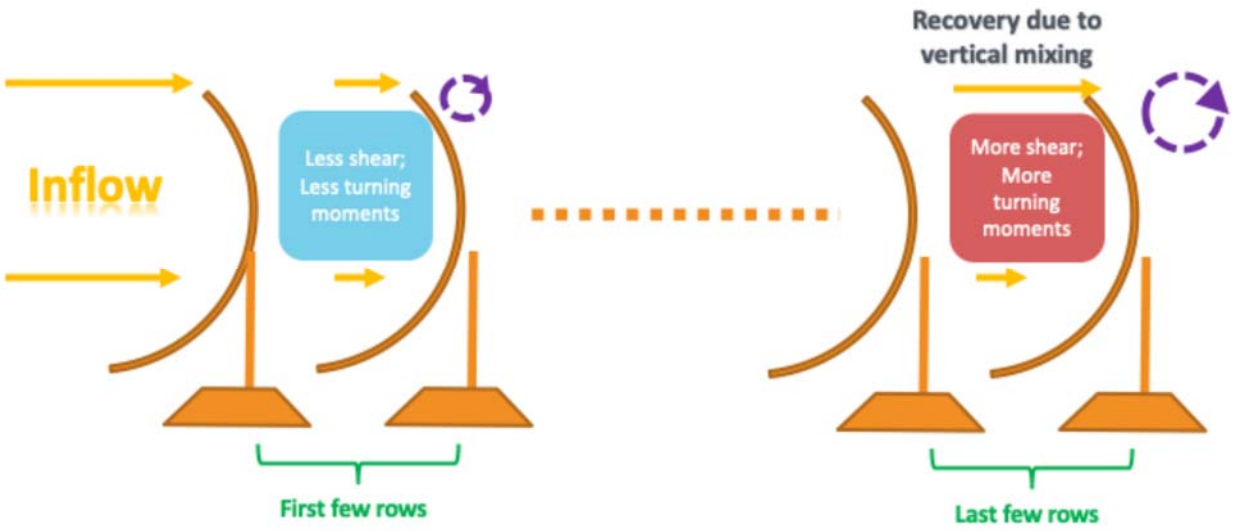

Figure 10: Schematic of the impact of increased wind shear normal to the ground on higher turning moments in the interior of the plant.

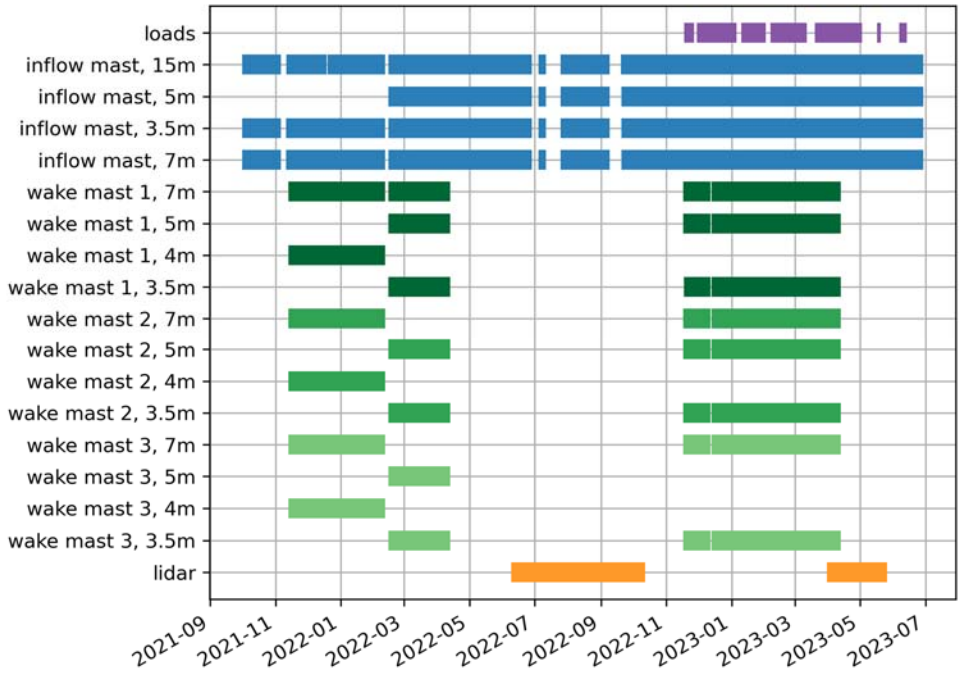

Figure 11: Timeline of wind and loads data acquisition at the NSO power plant.

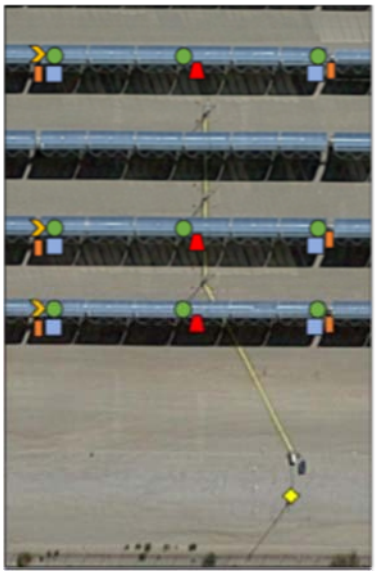

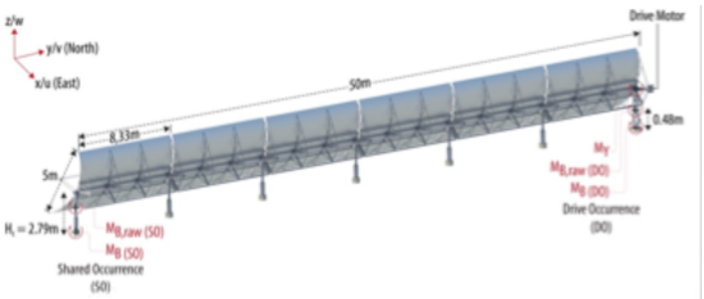

Key:

- Drive Torque
- Pylon Bending
- Dynamic Tilt
- Accelerations
- Mirror Vibration
- Wind Speed

Variable	Symbol	Description	Unit
Loads at row Z and location *loc* (Z=1,2 or 4; *loc* = DO, SO or Mid)			
RZ_*loc*_Bending	M_B	Bending moment at DO or SO	kNm
RZ_DO_Torque	M_T	Torque moment at DO	kNm
RZ_*loc*_Accel_X	a_x	Acceleration at spaceframe on western edge, perpendicular to mirror plane	g
RZ_*loc*_Accel_Y	a_y	Acceleration at spaceframe on western edge, in mirror plane	g
RZ_Disp_*pos*	d	Mirror displacement at westernmost, mid panel (*pos*=NW, NE, SW, SE or Center), zero-value subtracted	mm
RZ_Disp_*pos*_orig	d_0	Mirror displacement as above, absolute value	mm
RZ_*loc*_Tilt	α	Tilt of spaceframe at DO, Mid or SO	°
Anemometer	U	Wind speed at 15 m height (same as in wind data)	m/s
RZ_*loc*_C_Bending	C_{mb}	Bending moment coefficient at DO or SO	-
RZ_DO_C_Torque	C_{my}	Torque moment coefficient at DO	-
RZ_*loc*_Cfx	C_{fx}	Drag force coefficient at DO or SO	-

Figure 12: Schematic of the loads instrumentation installed on 3 rows of troughs at the NSO plant. Also shown is a table with all quantities being measured at 20 Hz frequency.

3.2 Static and dynamic support structure loads

The wind measurements at NSO are complemented by structural load measurements at the rows located near the met masts. Figure 11 provides an overview of the operating period of all individual wind and loads instruments. While the met mast and lidar configuration were slightly changed over the course of the measurement period and the loads instrumentation was first added in November 2022.

The load sensors were installed in rows 1, 2 and 4, close to the met mast locations, with loads instrumentation including support structure bending moments, drive torque moments, mirror deflections, dynamic tilt angles of the troughs, and accelerations at the space frame. The sensor locations on the space frame or trough mirrors are depicted in Figure 12 Figure 12: Schematic of the loads instrumentation installed on 3 rows of troughs at the NSO plant. Also shown is a table with all quantities being measured at 20 Hz frequency.along with a table listing measured and derived quantities. In this report, we focus on analyzing bending and torque moments for load coefficients, and tilt angles for torsional errors. Below, we analyze load coefficients for torque moment C_{my} (based on measured torque) and drag force C_{fx} (derived from measured bending moment):

$$C_{my} = \frac{M_y}{\frac{\rho}{2} U^2 \cdot L_{\text{panel}} \cdot W^2} \qquad C_{fx} = \frac{F_x}{\frac{\rho}{2} U^2 \cdot L_{\text{segment}} \cdot W}$$

M_y and F_x are the respective measured loads, U is the mean wind speed, ρ is the air density, L is the dimension of the trough segment or panel, and W is the aperture width.

The unique measurements at NSO offer a great opportunity to compare wind loads in idealized and commonly used wind tunnel tests against those observed in realistic operational power plant conditions. For this comparison, the large body of published data from the Hosoya tests [9] will be used. We compare drag and hinge moment coefficients, C_{fx} and C_{my} respectively, that were obtained in both the Hosoya and in the NSO study for winds perpendicular to the trough rows (western winds or 0° yaw angle).

Figure 13 shows the load coefficients for both studies in relation to trough angles for rows 1, 2, and 4. Trough angles are defined as zero at upward-facing toughs, negative at westward-facing troughs, and positive at eastward-facing troughs with the stow position 30° below the eastern horizon (120 °). The subplots include median values, averaged over all load coefficients at 10° (NSO), respectively 15° (Hosoya), trough angle bins. Additionally, peak minimum and maximum values for each trough angle bin are shown. The basic patterns observed for static loads align well with the wind tunnel results and are described below:

- Highest loads occur at the first row for both coefficients.
- The hinge moment coefficient at the first-row changes sign for trough angles facing up.
- Although drag coefficients are entirely positive at the first row, negative drag coefficients can occur in the second or fourth row at east- or west-facing troughs. As mentioned in the previous section, we believe eddies penetrating the flow field between the trough cause these fluctuations.

Additionally, mean C_{fx} values are significantly larger at NSO than observed by Hosoya. The stow position (120º) creates drag coefficients, even at rows 2 and 4, larger than what was observed in the study by Hosoya. Moreover, larger negative hinge moments at row 4 at east-facing trough angles, including stow, are observed.

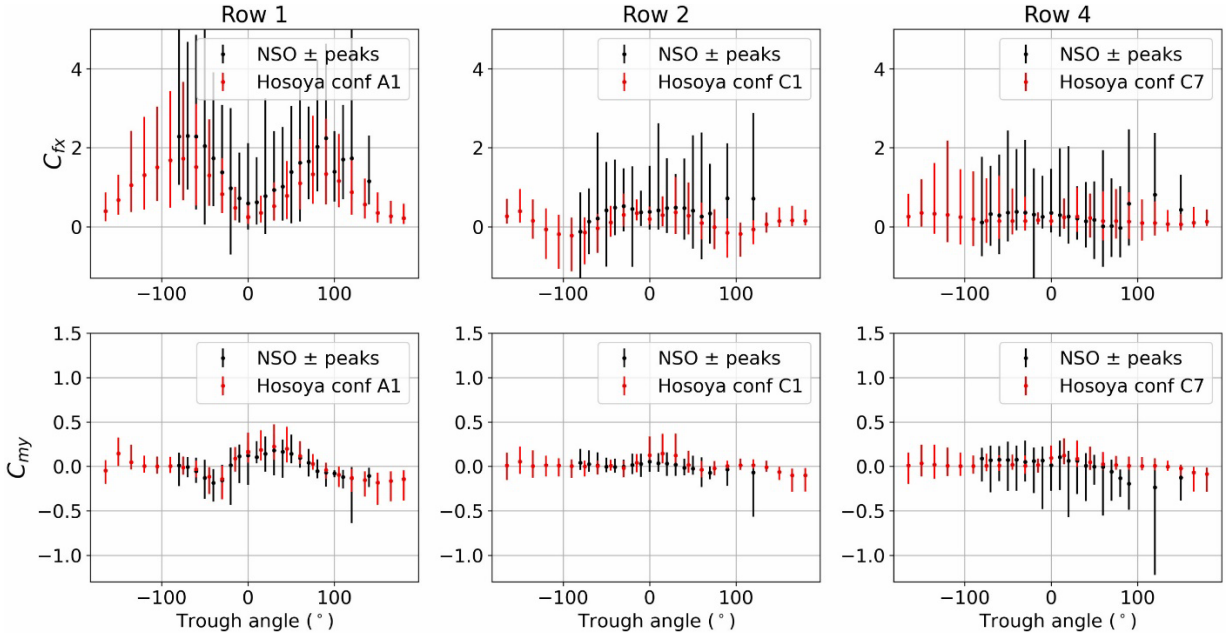

Figure 13: Comparison of drag and moment coefficient on all three rows against the Hosoya wind tunnel measurements.

In addition to static mean loads, the NSO measurements indicate higher peak loads compared to wind tunnel tests. This applies to all trough angles, row positions, and load coefficients, but is most pronounced for the drag coefficient. The discrepancy could be attributed to the fact that wind tunnel tests are conducted at defined wind speeds and TIs, whereas operational loads result from a broad range of these factors. This variability, especially at the 120º stow position, where the most data were collected, leads to a wider range of resulting peak loads. Notably, despite the higher TI at downstream rows, the first row still experiences the highest static and dynamic peak loads when considering all trough angles.

Higher peaks loads are observed at ~60º trough angles. The 60º trough angle is also most impacted by vortex shedding off the edges of the troughs. As an exception, row 4 sees remarkably high peak C_{my} values across all trough angles. A high-fidelity CFD model of the flow over parabolic trough rows [26] also observed increasing hinge moment variations at troughs located further into the field.

In general, trough angles ranging from approximately ±60º to ±90º appear to be most critical in terms of C_{fx} mean and peak loads at the first row, whereas angles of ±30º create highest static C_{my} loads with increased dynamic loads further into the field. This comparison clearly shows the need for more field measurements of static and dynamic loads as wind tunnel measurements are unable to fully reproduce the wide range of loads experienced by troughs in an operational power plant. Particularly, the interior rows of the field, which were not instrumented at NSO, should be studied in more detail.

Torsional loads on troughs

Wind-induced structural twist, or torsion, may deform the parabolic shape, thereby strongly reducing the optical performance of parabolic trough collectors (PTCs) as the heat flux from the collector is not fully captured by the absorber tube [27, 28]. Torsional misalignment can be mitigated through shorter trough segments or increased structural stiffness of the segments [29, 30].

Many studies of wind-induced torsion have relied on test bench experiments or numerical simulations. Based on numerical structural analysis, the wind-induced structural twist along the 100-m length of the LS-3 and EuroTrough collectors reaches 8 mrad at a wind speed of 11 m/s, resulting in 55 % of the heat flux missing the absorber tube [31, 32]. Further, numerical simulations have shown that turbulent wind can cause self-excited torsional vibrations for certain trough angles [33]. Wind-induced forces and displacements of the PTC increase with higher wind speeds, but by varying magnitudes depending on orientation [34].

Because the PTCs rotate throughout the day, the influence of orientation (tilt and yaw angle) on the wind-induced misalignment is important. Numerical results from a multiphysics-coupled transient model reveal maximum PTC displacement when the PTC faces away from the wind and minimum displacement when facing down [34]. Based on finite element analysis informed by wind pressure forces from wind tunnel experiments, the mirrors of a PTC experience a maximum peak displacement of 21.7 mm when the PTC is tilted 10 degrees away from the face-up position, toward the wind [35]. This peak displacement is located at the spanwise midpoint between the two support structures of the PTC. Overall, this study emphasizes the strong influence that PTC orientation has on the resulting forces, which is related to the windward exposed area, support structure, flow field and vortex shedding. Thus, understanding torsion along the PTC and how it varies with orientation and wind conditions, especially in an operational setting, is important in mitigating the resulting optical errors and maximizing performance.

In the current project, we characterized the torsion of the PTC support structure observed at three rows in the NSO CSP plant and assess the influence of wind loading in the torsional misalignment by investigating the following research questions:

1. How does torsional misalignment of PTC support structures vary over time and by location for three rows at an operational CSP plant?
2. How does wind loading affect the torsional misalignment?

Quantification of torsional misalignment and detailed understanding of its causes, as done in this study, can lead to targeted mitigation efforts including improved control strategies, system and component design, and performance models that will improve the performance, reliability and bankability of future CSP power plants.

Figure 14 illustrates how torsional error varies with tilt angle during strong, westerly winds (opaque) versus during weak winds from any direction (translucent). Here, the term “strong winds” refers to wind speeds greater than 4 m/s, “weak winds” refers to wind speeds less than 3 m/s, and “westerly” refers to wind directions between 225 and 315 degrees clockwise from north, which are perpendicular to the PTCs. The translucent markers illustrate the baseline angular misalignment without wind effects. Rows 1 and 2 experience a baseline torsional error of

approximately 10 mrad due to gravity, distance of the support pylon (shared occurrence, SO) from the drive (drive occurrence, DO), and variation in assembly or component (e.g., bearings) stiffness at the measurement locations. The absolute difference between the opaque and translucent markers represents the wind effects and eliminates the uncertainty associated with possible misalignment of the inclinometer mounting surfaces. The wind effects are the most noticeable in row 1 and diminish as one moves farther into the interior of the collector field. In all rows, the wind conditions impact the torsional error at angles between -20^o and +40^o, with maximum differences at 0 degrees in rows 2 and 4, which aligns with [27], who stated that “the face-up orientation is typically the most exposed and dangerous."

At zero or positive tilt angles, strong westerly winds change the median torsional error by up to 18 mrad in row 1, 8 mrad in row 2 and 6 mrad in row 4. At negative tilt angles less than -15 degrees, strong westerly winds change the median torsional error by up to 9 mrad in row 1, but do not affect the torsional error in rows 2 and 4. Compared to the weak wind condition results, which depict symmetric behavior about the peak in row 1, the strong westerly winds induce a dramatic asymmetry about this tilt angle of -15 degrees because of the parabolic shape. This critical tilt angle of -15 degrees aligns with the finite element analysis results from [35], who identified a maximum peak displacement of the mirrors when the PTC is tilted 10 degrees toward the wind from face-up.

These findings reveal a clear dependence of the torsional error on both tilt angle and wind conditions. During strong westerly winds, row 1 experiences a trend similar to that in rows 2 and 4 at positive angles but deviates dramatically at angles less than -15 degrees (more west-facing), which exemplifies the influence of the wind-induced deflection as the PTC exposes more interior surface area to the wind. This interaction between PTC orientation and the inflow wind is depicted in Figure 15. During weak winds, the SO location of row 1 lags behind the DO location by between 9 and 14 mrad (Figure 15 a,c). During strong, westerly winds, row 1 at SO lags behind DO even more, by up to 27 mrad when facing eastward ($\beta > 0$).

The peak row 1 torsional error at the 35-degree tilt angle coincides with the peak hinge moment [36], which indicates stronger aerodynamic forces acting on the upper part of the outer surface of the PTC at this position unlike when the PTC faces directly east ($\beta = 90^o$) and the forces acting on the upper part of the PTC are counteracted by those acting on the lower part. At tilt angles less than -15 degrees, the strong winds cause torsional error to drop to almost zero, indicating minimal twist in row 1. As depicted in Figure 15 (b, d), when the wind impinges on the outside, convex surface of the PTC, the aerodynamic force rotates the PTC to face more eastward. However, when the wind impinges on the inside, concave surface of the PTC, the same aerodynamic force results in rotating the PTC to face more westward. This stark difference between the strong and weak wind conditions at negative tilt angles does not appear in rows 2 or 4 because row 1 blocks the incoming wind.

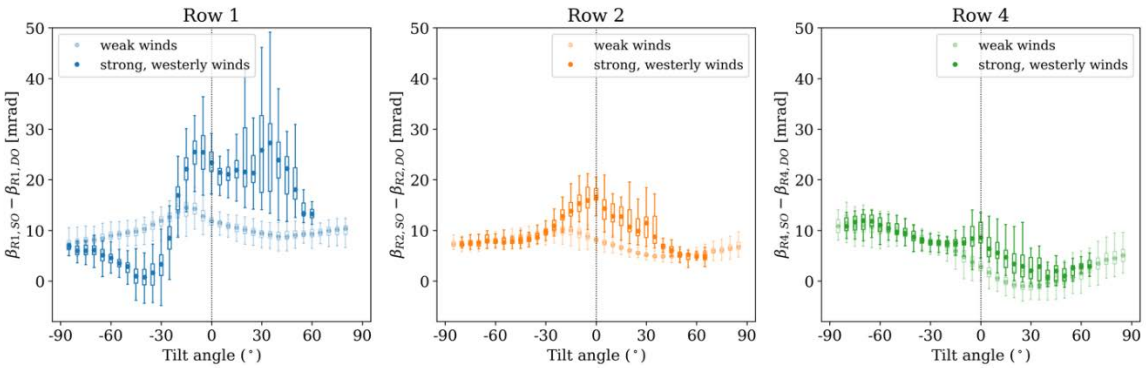

Figure 14: The relationship between torsional error at the shared location (SO) and tilt angle for strong wind conditions (opaque markers) versus weak wind conditions (translucent markers). Results are represented using box plots of all daytime, operational data from December 23, 2022, to June 11, 2023. Box plots shown only when the number of data points exceeds 20.

As shown in Figure 15, wind speed has the opposite effect on torsional error depending on PTC orientation when the row 1 PTC faces eastward versus westward. When the PTC faces east, which is pointed away from the incoming trough-perpendicular wind, the torsional error increases as wind speed increases because the aerodynamic forces rotate the PTC downward at the looser SO and Mid tilt sensor locations, increasing the lag between DO and SO. In contrast, when the PTC faces west, which is pointed toward the incoming wind, the torsional error decreases as wind speed increases, because the aerodynamic forces act on the inside of the PTC and push it downward, resulting in more downward rotation at the SO and Mid locations. Because the PTC is facing the wind, this downward rotation reduces the lag between DO and SO, as depicted in Figure 15. Flow simulations from previous studies [37, 38] illustrate the wind flow patterns that affect the PTC support structure stability and tracking system due to stronger eddies on the leeward side of the PTC when it faces the wind versus away from the wind. The wind's impact on torsion is stronger when the PTCs face away from the wind than when they face toward the wind, as highlighted by the steeper slope of the east-facing curve.

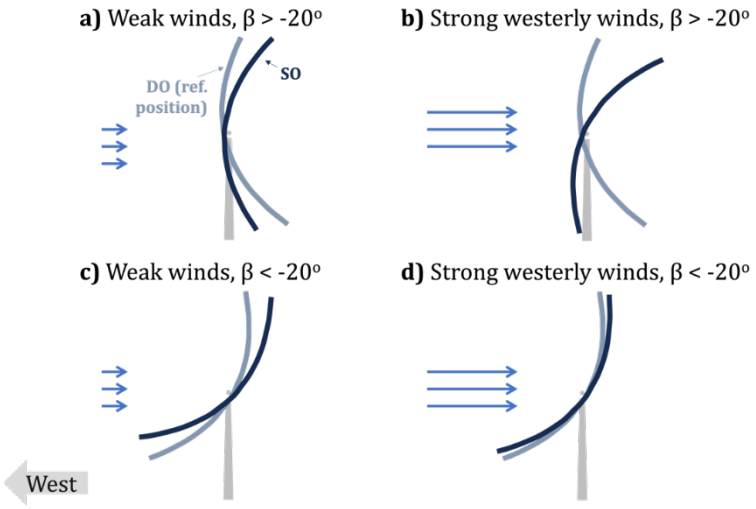

Figure 15: The angular displacement induced by weak winds versus strong westerly winds when the PTC faces away from the wind (β > -20°) versus toward the wind (β < -20°). Angular misalignment is exaggerated for clarity.

3.3 Wind and Loads measurement in a central tower power plant

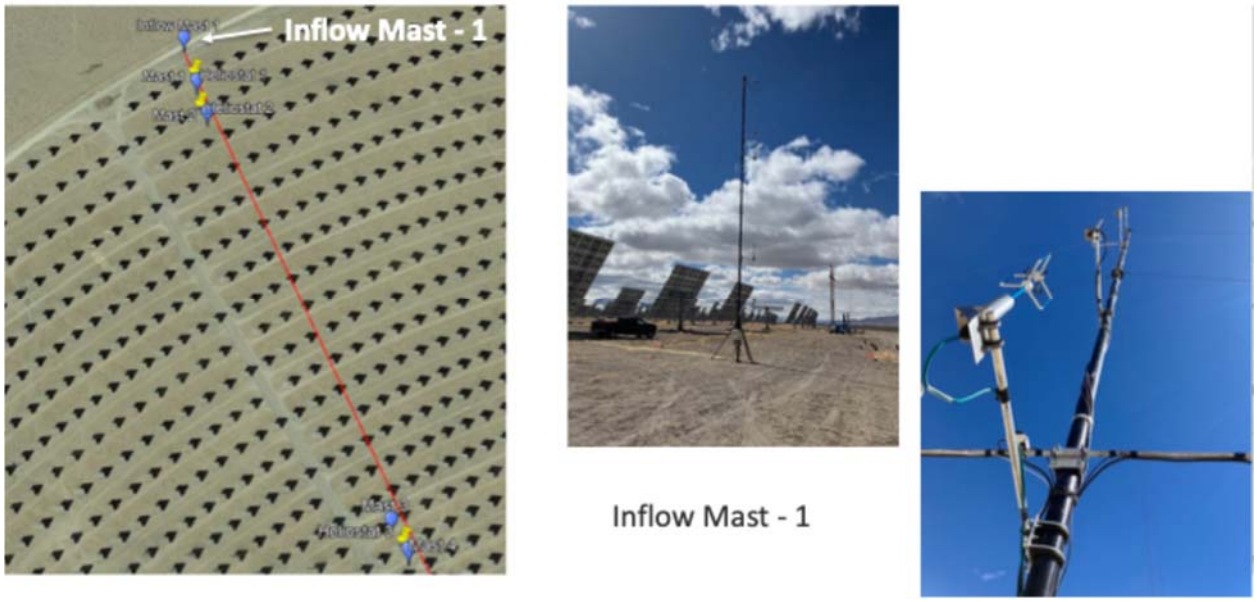

Figure 16: Inflow mast installed at Crescent Dunes power plant.

In addition to the parabolic trough plant, the NREL team installed wind and load measurement instrumentation in the heliostat field of the Crescent Dunes power plant. Data collection at Crescent Dunes started in March 2024 and is expected to continue through spring 2025. The dominant wind direction at the plant is from North, North-West. For this reason, the NREL team decided to focus on the North-West corner of the plant for the one-year campaign. The project team reused instrumentation from the NSO trough campaign and acquired some new instrumentation to characterize wind and loads at the N-W corner of the plant. The NREL team installed three met towers with three sonic anemometers on each of the towers in addition to the pressure, relative humidity and temperature sensors at the inflow tower. The sonic anemometers are installed at 2.75m, 5.5m and 11m. The 2.75m sonic anemometer is always shaded by the heliostat while the 5.5m sonic is on the hinge height level for the heliostats at Crescent Dunes. The 11m sonic is measuring wind above the upper edge of the heliostat.

Figure 17: Met tower upwind of the heliostats (one near the edge of the plant and other in the interior of the plant) equipped with load instrumentation.

Since the dominant wind direction at the plant is from N-W direction, the team installed one met tower outside of the N-W edge of the plant to measure the undisturbed flow of wind into the plant. Figure 16 shows this met tower, which will be referred to as the inflow tower. Two additional met towers with sonic anemometers at the same height as the inflow tower were also installed upstream of the heliostats with load instrumentation. This arrangement of wind measurement instrumentation ensured a high-resolution local characterization of the wind conditions encountered by the heliostats that were being continuously operated during the data collection time period. These met towers will be referred to as Mast-1 and Mast-2 in the remaining sections of this report. Each of the met towers was equipped with dataloggers and a cell phone modem that collects data at 20Hz frequency and transmits data to NREL servers every 3 minutes.

To characterize the global behavior of wind flow over the entire plant, a scanning lidar was installed on top of the heater bay adjacent to the center receiver tower. Figure 18, top left image, shows the location of the lidar installation. Figure 18 also shows the scanning lidar and the laser head movement. The height of the scanner head from ground level is 22.98m. Two sets of scanning patterns were applied for the wind data collection at the plant: range height indicator (RHI) and plan position indicator (PPI). In the case of RHI scans (vertical scans), the lidar keeps the azimuth angle fixed and the elevation angle is varied to get a vertical profile of wind over the radial distance, which extends beyond the plant boundaries.

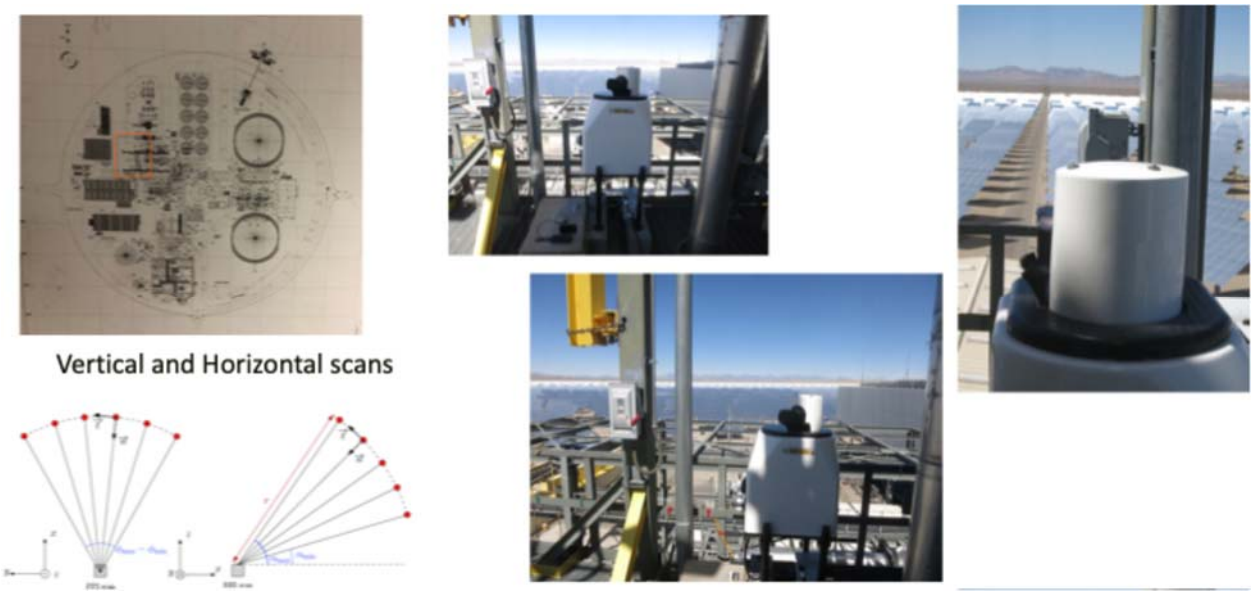

Figure 18: Scanning lidar installed on the heater bay at Crescent Dunes, along with a schematic of the scans performed every single minute.

With PPI scans (horizontal scans), the laser head remains at a constant horizontal elevation and scans in the azimuthal direction, producing profiles of wind as a function of radial distance from the lidar. Figure 19 shows representative RHI and PPI scans acquired on September 15th, 2024.

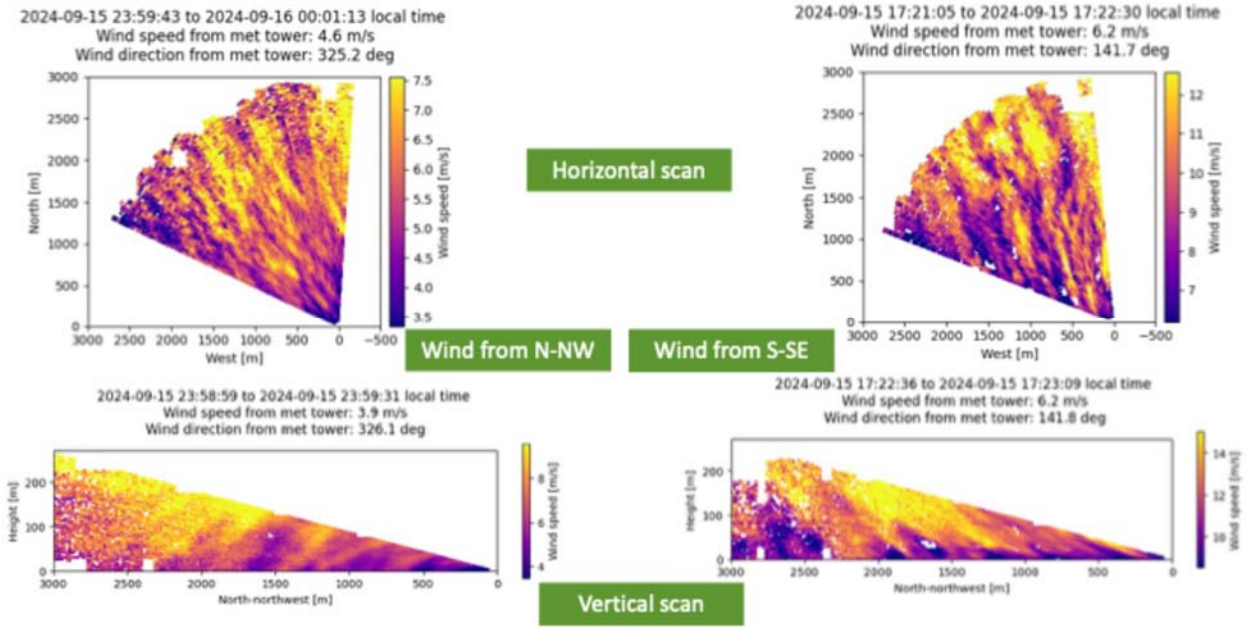

Figure 19: Wind profiles captured by PPI and RHI scans in two separate instances with differing wind conditions.

These four different scans show wind profiles during nighttime when wind was coming from the North (left bottom and top images) and during daytime with wind coming from the south (right top and bottom images). Both cases are captured with both RHI and PPI scans (top and bottom images in Figure 19). Simultaneous measurement of large-scale wind profiles using scanning

lidar and local high-resolution wind profiles using met towers provides us with a unique opportunity to construct a detailed picture of wind flow into the plant being modified by the heliostats. This kind of data has been never reported for power tower systems and will greatly benefit the CSP community in designing resilient solar fields.

The NREL team instrumented three heliostats, two at the N-W edge of the plant and one in the interior field. Figure 16 and Figure 17 show the location of the three heliostats that were instrumented with load instrumentation. All these three heliostats were instrumented with 25 separate instruments each. Figure 20 shows all the instruments installed on each of the three heliostats.

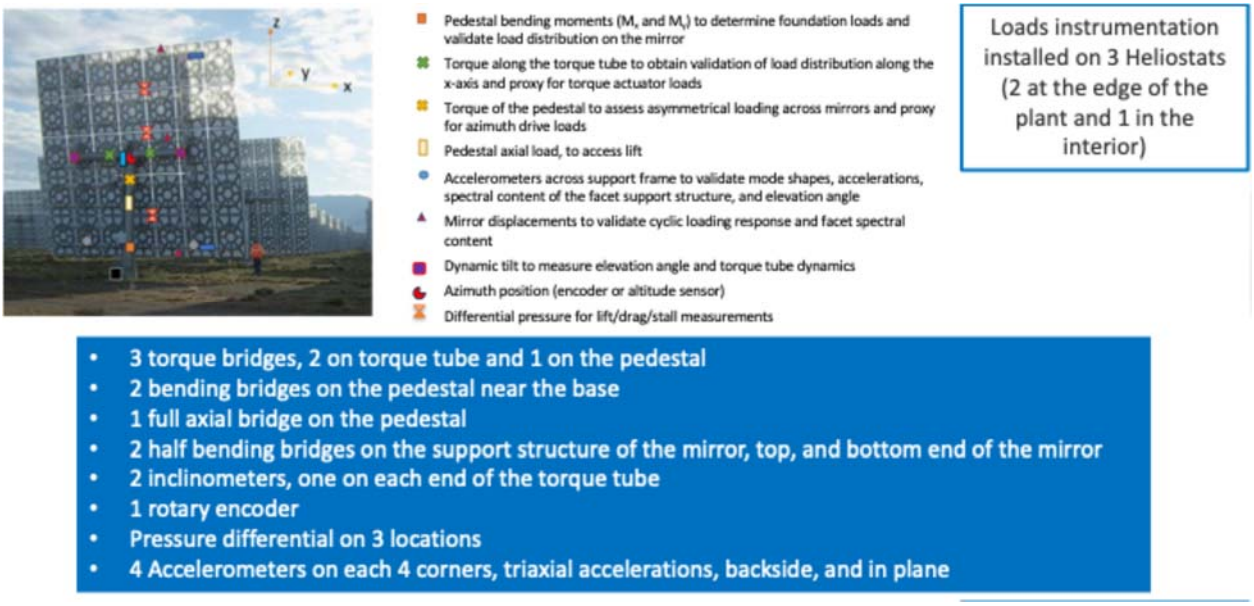

Figure 20: Load instrumentation installed on three heliostats at Crescent Dunes. Data is acquired continuously at 20 Hz frequency.

One of the critical sensors that we installed at Crescent Dunes, in addition to the otherwise similar instrumentation installed at NSO, are pressure differential sensors which provide the difference in atmospheric pressure observed on either side of the mirror surface. The project team installed three of these sensors on each of the heliostats. Data from these pressure differential sensors will generate critical information about the lift and drag forces experienced by the mirror surface. Static mean values and dynamic variation in terms of peak-to-peak values, while the heliostats are fully operational, will generate a unique dataset to help design next generation heliostats.

3.4 Wind shear in the plant interior and impact on turning moments on heliostats

Data acquisition at Crescent Dunes is still ongoing, but we have successfully started the analysis of preliminary data. Measuring wind and loads in the interior collector field at Crescent Dunes allows us to study wind shear and turning moments in the interior field. One of the critical conclusions derived from the NSO parabolic trough campaign was the presence of increased wind shear in the interior of the plant. This increased shear results in higher turning moments on

drives and supporting structures holding up the trough mirrors. This key insight was never highlighted in the literature and will impact the design of solar fields significantly. The project team wanted to confirm that a similar finding was observed on heliostats at Crescent Dunes. This was one of the key motivations for spreading the wind and load measurement instrumentation between the edge and the interior of the plant.

Figure 21 shows the wind shear, defined as the wind speed difference between the sonic anemometer measurements at 11m and 5.5m. Wind rose plots in Figure 21 are generated using the mean wind direction recorded at the 11m height with dominant wind direction being N- NW. Figure 21 shows that the highest wind shear, at heights corresponding to the upper edge of the heliostat assembly, is observed at the interior met tower. This wind shear observed in the interior will lead to higher turning moments on heliostat assemblies in the interior. Interior heliostats being shielded and therefore experiencing lower loads has been the solar field design philosophy. However, this observation of higher moments in the interior of the solar field, consistent with our findings in the parabolic trough plants, is counterintuitive and will lead to significant changes in solar field design.

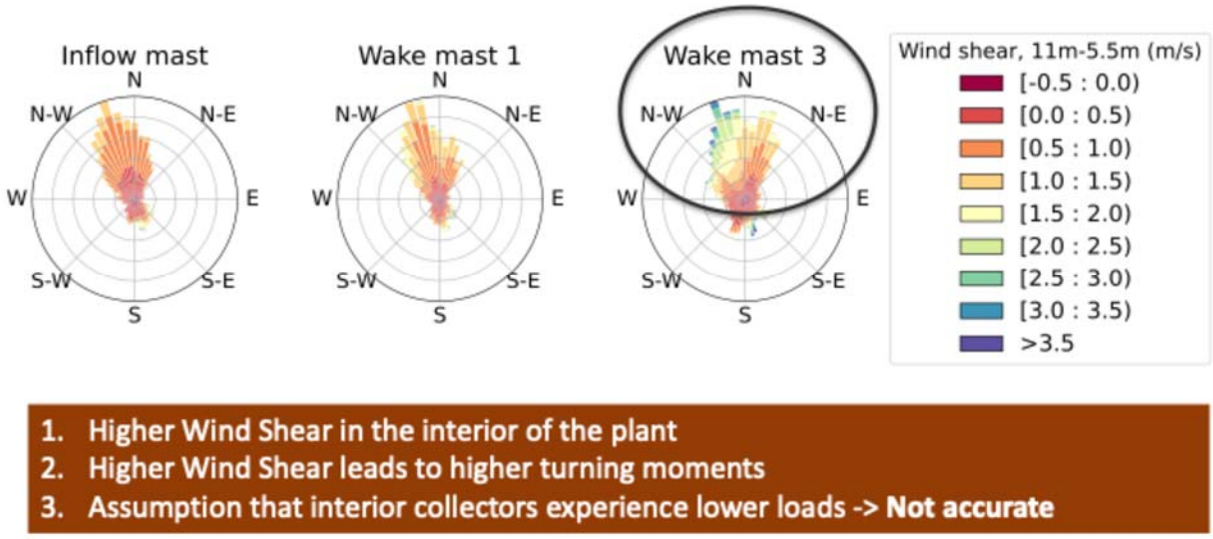

Figure 21: Increased wind shear observed in the plant's interior. This increased wind shear would lead to higher turning moments experienced by the heliostats in the interior of the plant.

One of the reasons behind commissioning complementary wind measurement instrumentation, met towers and a scanning lidar was to provide additional validation for each of the findings. The lidar vertical profile measurements (RHI scan) provide further information on the wind speed gradient in the collector field. Figure 22 shows the vertical profile of wind speed at various locations within the power plant from lidar scans. As shown in the figure, the gradient of wind speed steepens in the interior of the plant when compared against at the edge and outside of the plant. Vertical RHI scans on several other days, not shown here, confirm the increased gradient of wind speeds in the interior similar to the observations from the met tower. Analysis of the loads from the interior heliostat will be performed in the future to confirm the hypothesis of this increased wind shear in the interior of plant, leading to higher turning moments.

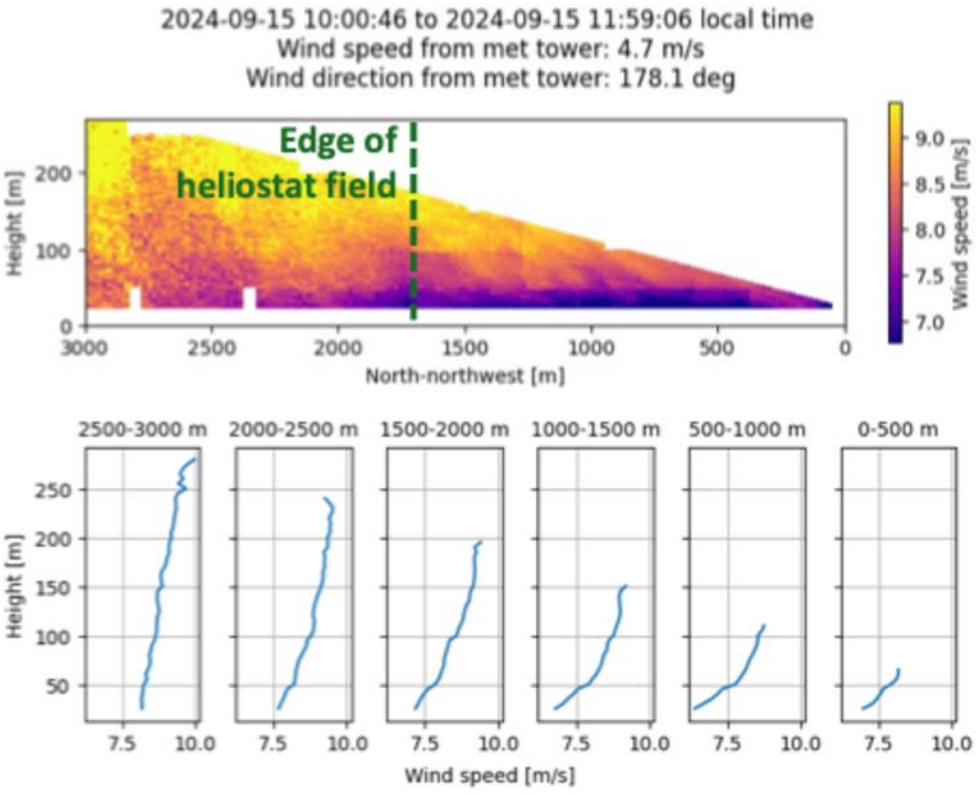

Figure 22: Wind speed field measured by the scanning lidar performing a vertical scan (RHI) on 15th September 2024. The bottom image shows the vertical profile of wind speed at various locations in the power plant and extending beyond the outer edges of the plant.

3.5 Development and validation of a simulation technique to model loads on solar collectors

To simulate unsteady aerodynamic loading on solar collectors with different geometries, in arbitrary solar field configurations, and under a variety of atmospheric conditions, a robust, easy to use, and computationally efficient modeling approach is critically needed. Structural responses to extreme conditions and during operating conditions associated with aeroelastic instabilities need to be predictable; deep-array and terrain effects on CSP structures are not well understood. Computational fluid dynamics may be applied to the problem, but the representation of solar collectors presents a unique challenge because their thicknesses are extremely small relative to the length scales of the atmospheric boundary layer (ABL). The ABL typically has heights on the order of a kilometer [42] with interior turbulence structures exerting time-varying forces and moments on structures immersed in the turbulent flow. These turbulence structures evolve from second to second and have integral length scales on the order of hundreds of meters [43]. To accurately capture the spatiotemporal evolution of turbulence within the ABL, large-eddy simulations (LESs) have been used for many decades within the atmospheric sciences community (since 1970 [44]).

The most rigorous but computationally intractable approach (for industrial applications) would be to use wall-resolved LES, where wall-resolved means that the flow around an exact representation of the solar collector geometry is captured. This would entail modeling the flow

field around the collector edges with enough resolution to capture the local stagnation at the leading edge of the collector, the surface laminar-to-turbulent transition and, depending on operating conditions, the flow separation point on the lee side of the collector. These are challenges faced by modelers in the aerospace field and problems to which detached eddy simulation or hybrid Reynolds Averaged Navier-Stokes / LES approaches have been successfully applied [45]. However, even those problems of interest that involve airfoils or wings have thicknesses that are an order of magnitude or more compared to our problem. For instance, a well-studied "thin" airfoil is the NACA0012 geometry, which has a thickness-to-chord ratio of 12%; in contrast, a representative heliostat may have a ratio of <<1% [46]. We therefore must develop a new simulation strategy.

Immersed boundary methods [47] have the promise of ease of use and flexibility for a variety of applications. There are two general approaches to implementing an immersed boundary: ghost cells and cut cells. To our knowledge, neither have been used for modeling such thin immersed bodies as solar collectors. Ghost cells, the simpler, more computationally efficient approach, entails manipulation of values in fictious parts of the mesh that reside within solid bodies and would necessarily require a computational mesh with points located within the thickness of a solar collector. In addition to this challenge, the more accurate cut-cell approach would have further increased cost to address possible numerical stability issues associated with flow near the thin immersed body.

We have developed two computationally efficient and viable solutions to the solar collector aerodynamic modeling problem. The first leverages actuator modeling, which is widely used for wind energy applications [48] and is readily available in DOE LES software [49]. The second develops a new thin immersed body approach, which will be briefly presented here.

Actuator Model

The actuator modeling approach (Figure 23) was implemented for solar collector modeling in two ways. The "steady" approach uses tabulated aerodynamic coefficients (of lift and drag) to represent the force exerted by the solar collector on the flow field. Starting from public domain airfoil data for the NACA0009 (9% thickness/chord ratio)—the most comprehensive high Reynolds number (representative of atmospheric flows) aerodynamics data available for a full range of angles of attack (0–90°)—we have verified that the lift and drag of a heliostat can be replicated using the steady actuator model in the linear and bluff body regimes. Note that the Reynolds numbers in the ORW15 and SN20 references are ~O(10^5), which are the highest available (aside from Emes et al. 2018 [50]) but still several times smaller than needed to achieve Reynolds number similarity in a real ABL. These two regimes correspond respectively to low angles of attack at which the lift coefficient C_l is known analytically; and high angles of attack at which aerodynamic lift vanishes, due to massive flow separation from the surface with the resulting forces dominated by drag.

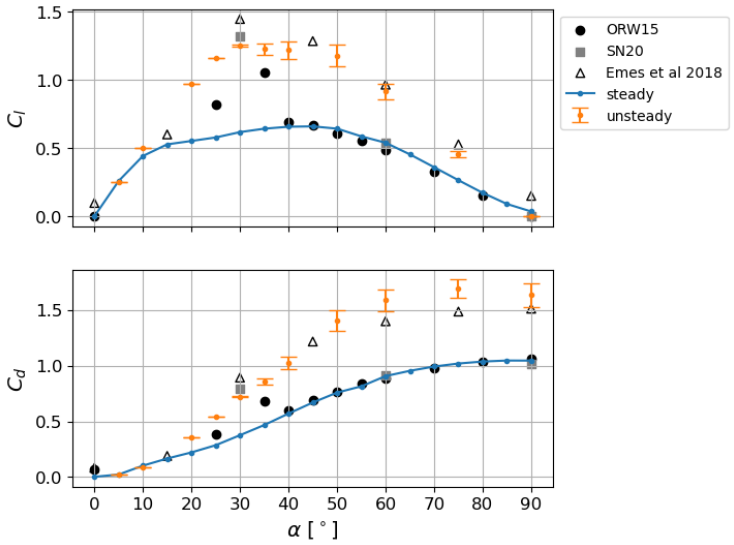

Figure 23: Coefficient of lift and drag as a function of angle of attack. The symbols are experimental data for a flat plate from [39, 40, 2]. Results titled steady and unsteady are data from the simulations model developed by the NREL team.

The intermediate regime is characterized by flow separation over a portion of the surface on the lee side, as opposed to massive flow separation from the entire surface. For thin lifting bodies, the flow will generally separate from the leading edge due to a large adverse pressure gradient. Subsequently, the flow may reattach on the aft portion of the body, constituting a separation bubble. These flow features are not captured by the steady approach because the actuator model imposes a force that represents the effect of the lifting body on the surround fluid but does not actually prevent flow from passing through the body itself. For wind turbine rotors, which have low solidity (i.e., the blockage from the blade area relative to the full rotor area), this is consistent with momentum theory and a minor technicality. However, for a solar collector this approach is less valid.

To enable "unsteady" actuator modeling, we eschew the tabulated aerodynamics and instead estimate the instantaneous local body force from the acceleration needed to drive the velocity normal to the solar collector to zero, i.e., enforce no penetration. For numerical stability, a relaxation factor less than one is applied, which approximately enforces the no-penetration condition. We see that the resulting lift and drag have validity over the full range of angles of attack and compares well with the reference dataset from Emes et al. 2018 [50] (with higher Reynolds number of 8.8×10^5, Figure 23).

Thin Immersed Body Model

To impose body forces in the actuator model approach, the point force exerted at the surface is cast as a distributed force on a region of cells in the vicinity of the surface. This force projection, typically applied through a normalized Gaussian weighting function, enhances numerical stability by mitigating the effect of imposing a discontinuous force field on the flow. However, it is this very discontinuity that achieves the flow separation that we seek to represent. The success of the actuator modeling approach depends on the appropriate selection of parameters that describe the Gaussian function [51] and is therefore not a turnkey solution. The aforementioned relaxation factor offers another source of uncertainty. Lastly, because the forces derived from the

no-penetration condition are projected over a subset of the flowfield volume, recovering the corresponding aerodynamic forces requires integration over a large volume that encloses the body, sampling from which is subject to additional discretization error and unwanted coupling to the aerodynamic influence of other nearby bodies. We therefore develop an alternative approach.

The thin immersed body model imposes a no-penetration, slip wall condition on the interior of the computational domain at the faces of computational cells that coincide with a modeled solar collector. This wall condition is accomplished by zeroing the fluxes through these faces and effectively models an immersed body with zero thickness. The thin immersed body model has been implemented within the DOE Energy Research & Forecasting (ERF) numerical weather prediction model that is currently under active and rapid development [52,53]; see also https://github.com/erf-model/erf. The choice of ERF was motivated by the ability to exactly impose zero flux through thin body surfaces, a numerical methodology (explicit timestepping) that is more compatible with imposing a discontinuity at thin-body surfaces, and GPU readiness. Furthermore, this model does not introduce any new modeling parameters, does not use a force projection and, consequently, permits a localized force reconstruction based on textbook control volume analysis.

Results for uniform inflow, i.e., turbulence intensity (TI) of 0%, show excellent agreement with expected trends relative to experimental reference data in the literature (Figure 24). For the 90° case (incident flow is perpendicular to the solar collector), a body-resolved flow simulation using the Exawind solver suite [49] was performed at the maximum resolution possible given limitations in computational resources. As such, the modeled heliostat was 2 cm thick, substantially thicker than the 3 mm experimental model from Australian Solar Thermal Research Institute (ASTRI, see Ref. 54). Even with the thicker body, the 29 million computational cells were needed to represent the flowfield around the heliostat geometry. (A thinner body would require even higher resolution near the body surface, and thus result in an even larger computational mesh.) This simulation required approximately 69,000 CPU-hours. In contrast, a comparable simulation using the thin body model (Figure 25) had only 1 million cells and was completed in 6.6 CPU-hours — a 10,000x speedup.

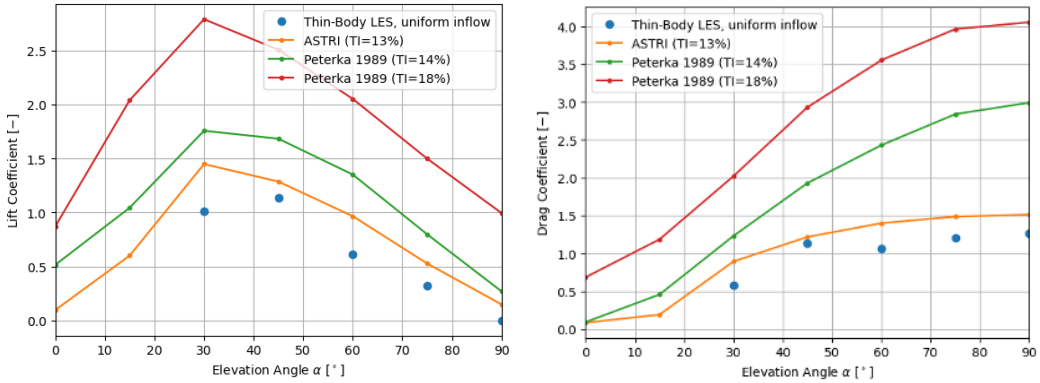

Figure 24. Comparison of the thin body LES model to heliostat data from Peterka et al. 1989 and ASTRI

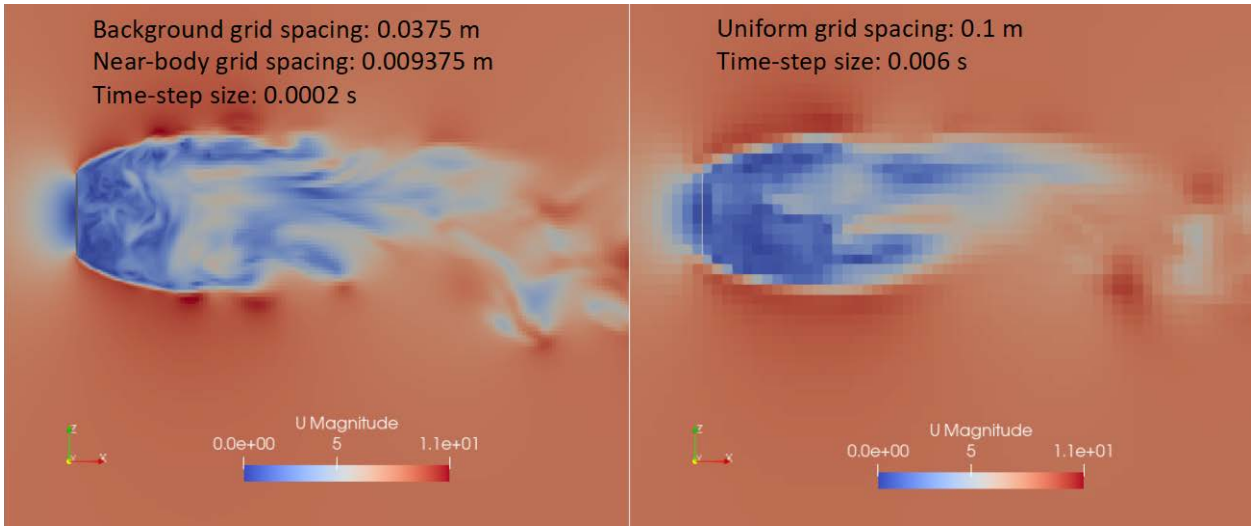

Figure 25: Comparison of wake behind a single heliostat computed using the computationally expensive body resolved mesh strategy (left image) and the computationally inexpensive thin body method (right image).

Lastly, we present results with the thin body model for the NSO experiment (Figure 26). We simulated 6 rows of parabolic trough collectors at different trough angles, focusing on the center of the solar field. Under inflow conditions with the wind normal to the troughs, we can represent this problem in 2D. The problem has been further simplified with uniform inflow. Even with these approximations, the loading characteristics on the front rows are captured well, with the simulated loads lying within the envelope of measurements at NSO at all three rows considered. Including turbulent ABL inflow will increase the unsteadiness of the loads, described by the standard deviation in drag (simulation error bars in Figure 26).

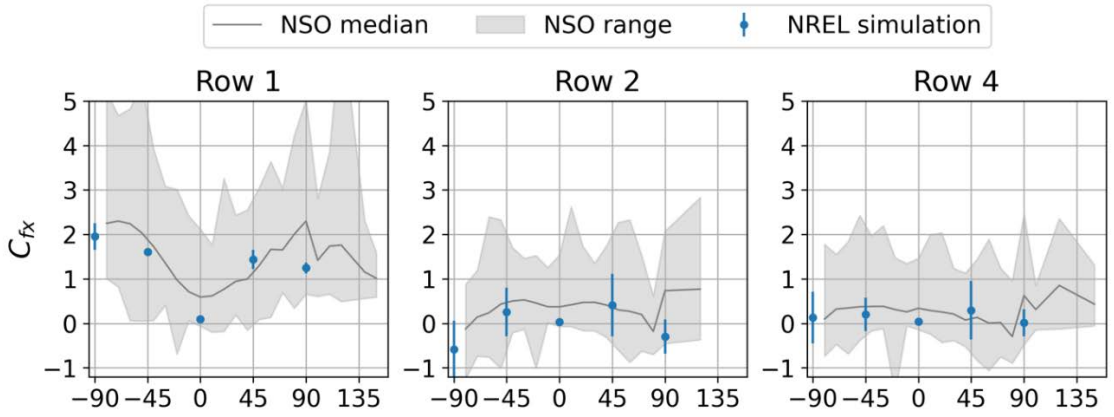

Figure 26: Comparison of drag coefficient C_{fx} collected at NSO and from the thin body simulations.

3.6 Simulation model capable of modeling dynamic deflections

To capture the dynamic deflections of the heliostats, we modified the software tool PVade[1] to enable CSP applications. PVade is a fluid-structure interaction software tool originally designed to simulate torsional galloping of solar photovoltaic (PV) panels. It is an open-source Python package that uses the open-source finite element package FEniCSx (Wells et al. 2021). PVade can be used both on a laptop and on high-performance computing clusters. To simulate the required physics, PVade employs a fractional step method to solve the arbitrary Lagrangian-Eulerian (ALE) incompressible Navier-Stokes equations. To model the structural response, PVade uses a partitioned fluid-structure interaction (FSI) coupling in which fluid and structure are solved separately and coupled through boundary conditions. The modified PVade software that enables simulation of heliostats has been merged into the open-source GitHub repository for public use.

In this study, we simulate a Crescent Dunes heliostat at three positions experiencing four mean wind speeds. We extract three positions of the outer heliostat at Crescent Dunes on March 14, 2024: stow, morning, and evening. The positions are shown in Figure 27 and Table 1. The four wind speeds include 2 m/s, 4 m/s, 6 m/s, and 8 m/s. For each case, simulating 20 seconds required about 4.5 hours on high-performance computing clusters.

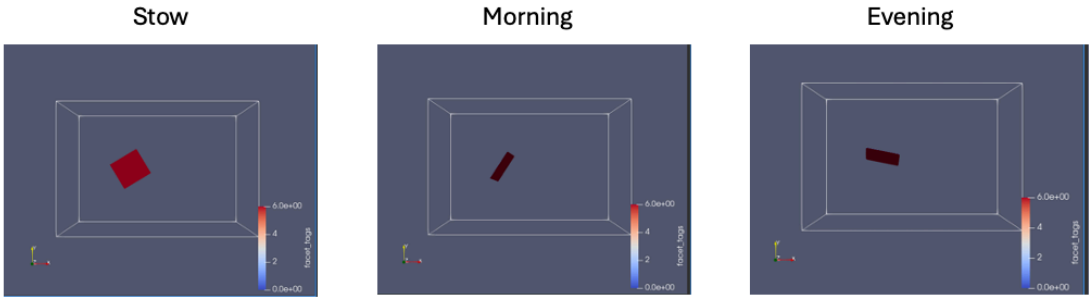

Figure 27: Top-down views of three heliostat positions used in simulations.

Table 1: Time and orientation details for three heliostat positions.

Case Name	Time (UTC)	Azimuth Angle (degrees)	Elevation Angle (degrees)
Stow	2024-03-14 12:00:00	149.0515	90.0227
Morning	2024-03-14 16:00:00	122.9065	14.8238
Evening	2024-03-14 23:30:00	191.2118	22.9154

The simulation results are shown in Figures 28 and 29. On the left of Figure 28, flow is moving from left to right and we see a snapshot of vortex shedding downstream of the heliostat. On the right, the gray scale represents the deformation experienced by the heliostat as a result of the surrounding flow. Figure 29 illustrates the time-series deformation of one corner of the heliostat over 20 seconds. The structural response is different for each wind speed and each heliostat orientation. The simulations of the heliostats in the morning and evening at high wind speeds ($u \geq 6$ m/s) fail because the deflections become unstable. These examples of the fluid-structure interaction elucidate the difficulty of simulating such a phenomenon.

[1] https://github.com/NREL/PVade

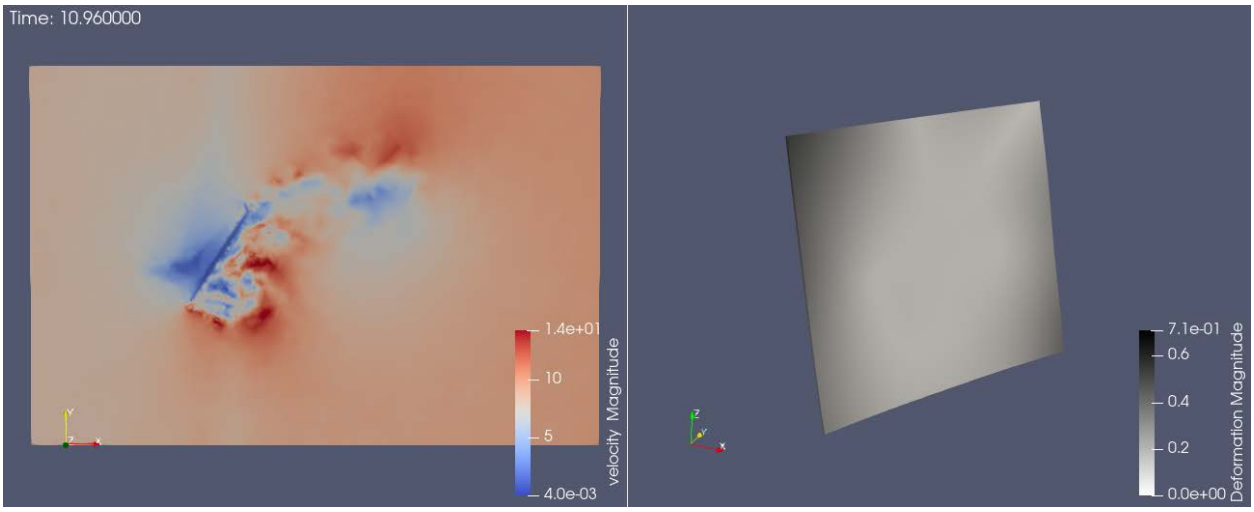

Figure 28: Snapshot of simulation results showing wind speed on the left and deformation of the heliostat on the right.

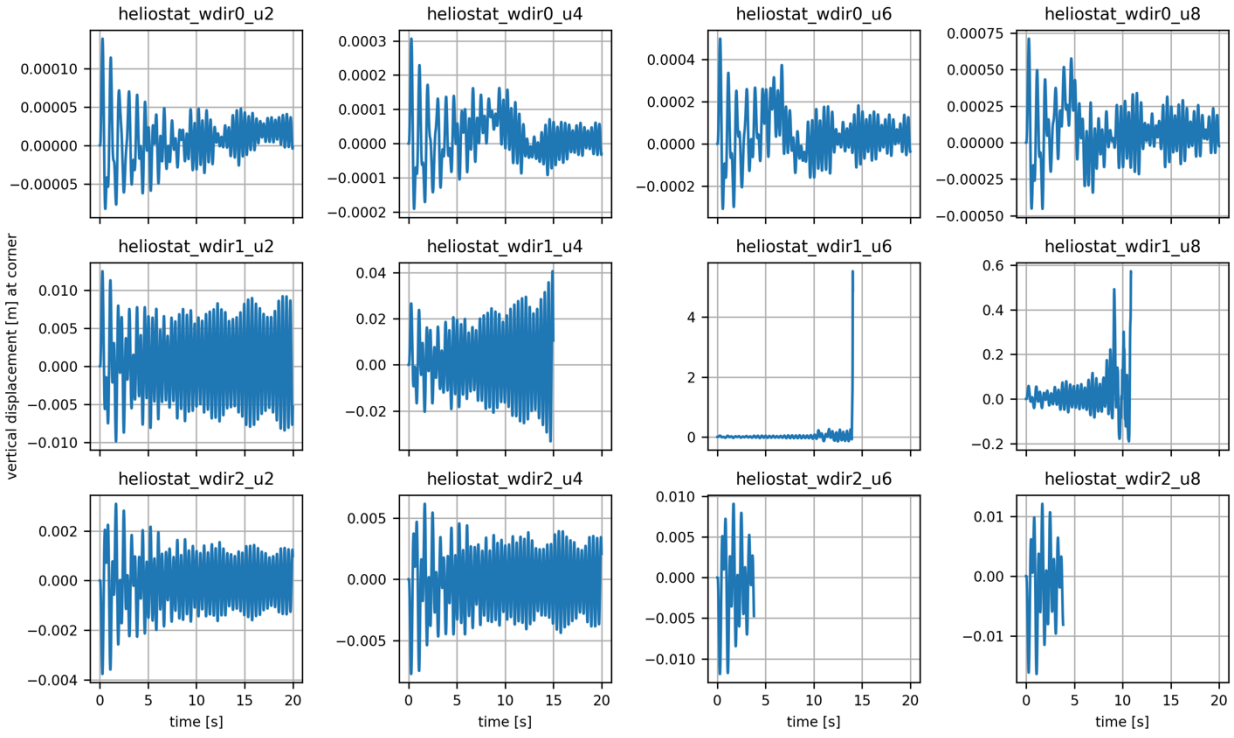

Figure 29: Time-series of vertical displacement at a corner of the heliostat in three orientations (rows) and experiencing four wind speeds (columns).

Figure 30 depicts the power spectral density of the dynamic deflections of the heliostat under the simulated environmental and operational conditions. This frequency analysis indicates which frequencies contribute the highest energy to the structural response. In general, as wind speed increases, energy increases. The orientation experiencing the highest energy occurs in the evening whereas the stowed position results in the lowest energy. The maximum energy peak in all cases occurs close to 2 Hz, which aligns with the peak energy frequency found in the field data from Crescent Dunes. The local maxima thereafter are similar in the stow and evening

orientations, but differ in the morning orientation. These results illustrate the software tool's effectiveness in simulating the dynamic deflections of heliostats and take the first step in understanding dynamic wind-driven loads in CSP solar collectors.

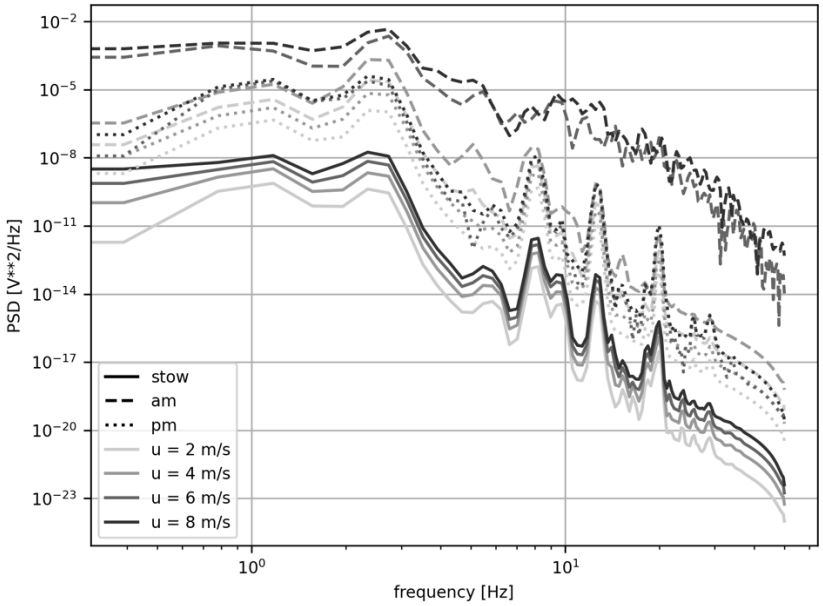

Figure 30: Power spectral density versus frequency of all simulated cases.

4 Significant Accomplishments and Conclusions

1. First-of-a-kind, comprehensive, high-resolution wind-loading datasets from two operational CSP plants.
2. Released fully validated open-source and computationally efficient tool for modeling wind loading on CSP collector structures. This CFD modeling tool was validated against wind tunnel heliostat data and parabolic data from the field over a wide range of angle of attacks. Moreover, we demonstrated reduced computational expense for modeling ~ 10 cpu-hrs/simulation.
3. Enabled simulation of dynamic wind loading of heliostats using a fluid-structure interaction software tool that can be run on a laptop or on high-performance computing clusters.
4. Analysis of wind driven loading datasets highlighted potential generation of higher vertical wind shear, potentially leading to increased turning moments deep in the field. Additionally, parabolic trough data from NSO revealed higher dynamic loads in the field data compared to wind tunnel data typically used for collector design. These never before highlighted conclusions will have significant impact on how future collectors and solar fields will be designed.
5. Quantified torsional loads on troughs in the field leading to intercept factors << 1.

5 Path Forward

The following are the steps that the project team is currently undertaking:

1. Detailed characterization of wind-driven loads on smaller-size heliostats. Along with the data from Crescent Dunes, this additional dataset will clarify the role of the size of heliostats and the height above the ground.
2. Study the impact of dynamic loading on structural life and optical performance of heliostats, both at Crescent Dunes and smaller heliostat installations.
3. Development of best practices and standards for measuring loads on CSP collectors in the solar field of existing or newer plants under development. Focus will be on generating guidance for collecting and utilizing wind & loads data during power plant operation to develop better stowing strategies and improve overall performance.
4. Develop guidance for generating design codes for qualification/certification of support structures specific to solar collectors. This collaborative activity will be with SolarPACES Task 3 and the PV industry where these codes will be similarly applicable.

6 Products

1. Wind loading dataset from the NSO parabolic trough plant uploaded to Open Energy Data Initiative (OEDI), doi: 10.25984/2001061. Dataset can be found at https://www.osti.gov/dataexplorer/biblio/dataset/2001061.
2. A similar dataset is under preparation using the data collected at Crescent Dunes.
3. Nature Scientific Data paper titled “Wind and structural loads data measured on parabolic trough solar collectors at an operational power plant”, Scientific Data 11, 98 (2024), https://doi.org/10.1038/s41597-023-02896-4
4. Solar Energy journal article titled “Field measurements reveal insights into the impact of turbulent wind on loads experienced by parabolic trough solar collectors”, Solar Energy, Volume 280, 2024, 112860, https://doi.org/10.1016/j.solener.2024.112860.
5. Six presentations at the SolarPACES conferences in 2022, 2023, and 2024
6. Two presentations at ASME ES conference in 2023 and 2024. One overview presentation at SPIE conference on Nonimaging Optics: Efficient Design for Illumination and Concentration XIX.

7 Project Team and Roles

1. Shashank Yellapantula – Principal Investigator
2. Ulrike Egerer and Matt Emes – Wind conditions and loads data analysis
3. Geng Xia and Aliza Abraham – Lidar data analysis.
4. Eliot Quon and Brooke Stanislawski – Simulation of wind loading on heliostats and parabolic troughs.
5. Brooke Stanislawski – Modeling of optical loss due to wind driven loads on parabolic troughs.
6. Scott Dana, Jerry Hur, Brian Manoa, Mark Iverson, and Tyler Cary – Loads measurement instrumentation on troughs and heliostats.
7. David Jager, Simon Thao, Mark Iverson, and Andrew Scholbrock – Wind measurement instrumentation at NSO and Crescent Dunes power plant.

8 References

1. Sun, H., Gong, B., & Yao, Q. (2014). A review of wind loads on heliostats and trough collectors. Renewable and Sustainable Energy Reviews, 32, 206-221.
2. Emes, M., Jafari, A., Pfahl, A., Coventry, J., & Arjomandi, M. (2021). A review of static and dynamic heliostat wind loads. Solar Energy, 225, 60-82.
3. Peterka, J. A., Hosoya, N., Bienkiewicz, B., & Cermak, J. E. (1986). Wind load reduction for heliostats (No. SERI/STR-253-2859). Colorado State Univ., Fort Collins, CO (United States).
4. Sment, J., & Ho, C. K. (2014). Wind patterns over a heliostat field. Energy Procedia, 49, 229-238.
5. Emes, M. J., Jafari, A., Coventry, J., & Arjomandi, M. (2020). The influence of atmospheric boundary layer turbulence on the design wind loads and cost of heliostats. Solar Energy, 207, 796-812.
6. Arango, J. F. V. (2016). Dynamic Wind Loads on Heliostats (Doctoral dissertation, Universitätsbibliothek der RWTH Aachen).
7. Jafari, A., Emes, M., Cazzolato, B., Ghanadi, F., & Arjomandi, M. (2020). Turbulence characteristics in the wake of a heliostat in an atmospheric boundary layer flow. Physics of Fluids, 32(4).
8. Ho, C. K., Griffith, D., Sment, J. N. I., Moya, A. C., & Hunter, P. (2012). Dynamic testing and analysis of heliostats to evaluate impacts of wind on optical performance and structural fatigue (No. SAND2012-8380C). Sandia National Lab.(SNL-NM), Albuquerque, NM (United States).
9. Hosoya, N., Peterka, J. A., Gee, R. C., & Kearney, D. (2008). Wind Tunnel Tests of Parabolic Trough Solar Collectors: March 2001--August 2003 (No. NREL/SR-550-32282). National Renewable Energy Lab.(NREL), Golden, CO (United States).
10. Randall, D. E., McBride, D. D., & Tate, R. E. (1980). Steady-state wind loading on parabolic-trough solar collectors (No. SAND-79-2134). Sandia National Lab.(SNL-NM), Albuquerque, NM (United States).
11. Winkelmann, U., Kämper, C., Höffer, R., Forman, P., Ahrens, M. A., & Mark, P. (2020). Wind actions on large-aperture parabolic trough solar collectors: Wind tunnel tests and structural analysis. Renewable Energy, 146, 2390-2407.
12. Azadeh, M., & Tavakol, M. M. (2021). Study of wind loading and flow characteristics on an array of parabolic trough collectors. Journal of Wind Engineering and Industrial Aerodynamics, 216, 104716.
13. Gong, B., Wang, Z., Li, Z., Zhang, J., & Fu, X. (2012). Field measurements of boundary layer wind characteristics and wind loads of a parabolic trough solar collector. Solar energy, 86(6), 1880-1898.
14. Paetzold, J., Cochard, S., Fletcher, D. F., & Vassallo, A. (2015). Wind engineering analysis of parabolic trough collectors to optimise wind loads and heat loss. Energy Procedia, 69, 168-177.

15. Guha, T. K., Fewless, Y., & Banks, D. (2015). Effect of panel tilt, row spacing, ground clearance and post-offset distance on the vortex induced dynamic loads on fixed tilt ground mount photovoltaic arrays. In 14th International Conference on Wind Engineering.
16. Strobel, K., & Banks, D. (2014). Effects of vortex shedding in arrays of long inclined flat plates and ramifications for ground-mounted photovoltaic arrays. *Journal of Wind Engineering and Industrial Aerodynamics*, *133*, 146-149.
17. Dupont, S., Gosselin, F., Py, C., De Langre, E., Hemon, P., & Brunet, Y. (2010). Modelling waving crops using large-eddy simulation: comparison with experiments and a linear stability analysis. Journal of Fluid Mechanics, 652, 5-44.
18. Lüpfert, E., Geyer, M., Schiel, W., Esteban, A., Osuna, R., Zarza, E., & Nava, P. (2001, April). Eurotrough design issues and prototype testing at PSA. In International Solar Energy Conference (Vol. 16702, pp. 387-391). American Society of Mechanical Engineers.
19. Sartori, F. T., & Heimsath, A. (2019, July). FEA study of innovative solutions for parabolic trough collector design. In AIP Conference Proceedings (Vol. 2126, No. 1). AIP Publishing.
20. American Society of Civil Engineers. (2017, June). Minimum design loads and associated criteria for buildings and other structures. American Society of Civil Engineers.
21. Bou-Zeid, E., Anderson, W., Katul, G. G., & Mahrt, L. (2020). The persistent challenge of surface heterogeneity in boundary-layer meteorology: a review. Boundary-Layer Meteorology, 177, 227-245.
22. Grant, E. R., Ross, A. N., Gardiner, B. A., & Mobbs, S. D. (2015). Field observations of canopy flows over complex terrain. Boundary-Layer Meteorology, 156, 231-251.
23. Pfahl, A. (2018). Wind loads on heliostats and photovoltaic trackers (Doctoral dissertation).
24. Sment, J., & Ho, C. K. (2014). Wind patterns over a heliostat field. Energy Procedia, 49, 229-238.
25. Blume, K., Röger, M., & Pitz-Paal, R. (2023). Full-scale investigation of heliostat aerodynamics through wind and pressure measurements at a pentagonal heliostat. Solar Energy, 251, 337-349.
26. Yellapantula, S., Vijayakumar, G., Kesseli, D., Ananthan, S., & Mehos, M. (2022, May). Aerodynamic analysis of wind loading on parabolic trough collectors using high-fidelity CFD modeling. In AIP Conference Proceedings (Vol. 2445, No. 1). AIP Publishing.
27. Mehos, M., Price, H., Cable, R., Kearney, D., Kelly, B., Kolb, G., & Morse, F. (2020). Concentrating solar power best practices study (No. NREL/TP-5500-75763). National Renewable Energy Lab.(NREL), Golden, CO (United States); Solar Dynamics, LLC, Denver, CO (United States).
28. Murphy, L. M. (1980). Wind loading on tracking and field-mounted solar collectors (No. SERI-TP-632-958). Solar Energy Research Inst.(SERI), Golden, CO (United States).

29. Weinrebe, G., Abul-Ella, Z., & Schiel, W. (2011, September). On the influence of parabolic trough collector stiffness and length on performance. In SolarPACES Conference, Granada, Spain (pp. 15-18).

30. Winkelmann, U., Kämper, C., Höffer, R., Forman, P., Ahrens, M. A., & Mark, P. (2020). Wind actions on large-aperture parabolic trough solar collectors: Wind tunnel tests and structural analysis. *Renewable Energy*, *146*, 2390-2407.

31. Lüpfert, E., Geyer, M., Schiel, W., Esteban, A., Osuna, R., Zarza, E., & Nava, P. (2001, April). Eurotrough design issues and prototype testing at PSA. In International Solar Energy Conference (Vol. 16702, pp. 387-391). American Society of Mechanical Engineers.

32. Sun, H., Gong, B., & Yao, Q. (2014). A review of wind loads on heliostats and trough collectors. Renewable and Sustainable Energy Reviews, 32, 206-221.

33. Andre, M., Péntek, M., Bletzinger, K. U., & Wüchner, R. (2017). Aeroelastic simulation of the wind-excited torsional vibration of a parabolic trough solar collector. Journal of Wind Engineering and Industrial Aerodynamics, 165, 67-78.

34. Zhang, Z., Sun, J., Wang, L., & Wei, J. J. (2020). Multiphysics-coupled study of wind load effects on optical performance of parabolic trough collector. Solar Energy, 207, 1078-1087.

35. Zou, Q., Li, Z., Wu, H., Zou, F., & Wu, B. (2019). Wind-induced response and pedestal internal force analysis of a Trough Solar Collector. *Journal of Wind Engineering and Industrial Aerodynamics*, *193*, 103950.

36. Egerer, U., Dana, S., Jager, D., Xia, G., Stanislawski, B. J., & Yellapantula, S. (2024). Wind and structural loads data measured on parabolic trough solar collectors at an operational power plant. Scientific Data, 11(1), 98.

37. Hachicha, A. A., Rodríguez, I., Castro, J., & Oliva, A. (2013). Numerical simulation of wind flow around a parabolic trough solar collector. Applied energy, 107, 426-437

38. Naeeni, N., & Yaghoubi, M. (2007). Analysis of wind flow around a parabolic collector (1) fluid flow. Renewable Energy, 32(11), 1898-1916.

39. Ortiz, X., Rival, D., & Wood, D. (2015). Forces and moments on flat plates of small aspect ratio with application to PV wind loads and small wind turbine blades. Energies, 8(4), 2438-2453.

40. Shademan, M., & Naghib-Lahouti, A. (2020). Effects of aspect ratio and inclination angle on aerodynamic loads of a flat plate. Advances in Aerodynamics, 2, 1-23.

41. ESDU 85020: Characteristics of Atmospheric Turbulence Near the Ground. Part II: Single Point Data for Strong Winds (Neutral Atmosphere), Data Item, Amendment (G), 978-0-85679-526-8, Engineering Sciences Data Unit (ESDU) (2001)

42. Stull, R. B. (1988). An Introduction to Boundary Layer Meteorology. Springer Netherlands.

43. Thedin, R., Quon, E., Churchfield, M., & Veers, P. (2022). Investigations of Correlation and Coherence in Turbulence from a Large-Eddy Simulation. *Wind Energ. Sci*, 8(4), 487–502. https://doi.org/10.5194/wes-2022-71

44. Deardorff, J. W. (1970). A numerical study of three-dimensional turbulent channel flow at large Reynolds numbers. *Journal of Fluid Mechanics*, *41*(2), 453–480. https://doi.org/10.1017/S0022112070000691

45. Spalart, P. R. (2009). Detached-Eddy Simulation. *Annual Review of Fluid Mechanics*, *41*(1), Article 1. https://doi.org/10.1146/annurev.fluid.010908.165130

46. Emes, M. J., Arjomandi, M., Ghanadi, F., & Kelso, R. M. (2017). Effect of turbulence characteristics in the atmospheric surface layer on the peak wind loads on heliostats in stow position. *Solar Energy*, *157*, 284–297. https://doi.org/10.1016/j.solener.2017.08.031

47. Verzicco, R. (2023). Immersed Boundary Methods: Historical Perspective and Future Outlook. *Annual Review of Fluid Mechanics*, *55*(Volume 55, 2023), 129–155. https://doi.org/10.1146/annurev-fluid-120720-022129

48. Sørensen, J. N., & Shen, W. Z. (2002). Numerical Modeling of Wind Turbine Wakes. *Journal of Fluids Engineering*, *124*(2), 393–399. https://doi.org/10.1115/1.1471361

49. Sharma, A., Brazell, M. J., Vijayakumar, G., Ananthan, S., Cheung, L., deVelder, N., Henry de Frahan, M. T., Matula, N., Mullowney, P., Rood, J., Sakievich, P., Almgren, A., Crozier, P. S., & Sprague, M. (2024). ExaWind: Open-source CFD for hybrid-RANS/LES geometry-resolved wind turbine simulations in atmospheric flows. *Wind Energy*, *27*(3), 225–257. https://doi.org/10.1002/we.2886

50. Emes, M. J., Ghanadi, F., Arjomandi, M., & Kelso, R. M. (2018). Investigation of peak wind loads on tandem heliostats in stow position. *Renewable Energy*, *121*, 548–558. https://doi.org/10.1016/j.renene.2018.01.080

51. Martínez-Tossas, L. A., Churchfield, M. J., & Meneveau, C. (2017). Optimal smoothing length scale for actuator line models of wind turbine blades based on Gaussian body force distribution. *Wind Energy*, *20*(6), Article 6. https://doi.org/10.1002/we.2081

52. Almgren, A., Lattanzi, A., Haque, R., Jha, P., Kosovic, B., Mirocha, J., Perry, B., Quon, E., Sanders, M., Wiersema, D., Willcox, D., Yuan, X., & Zhang, W. (2023). ERF: Energy Research and Forecasting. *Journal of Open Source Software*, *8*(87), 5202. https://doi.org/10.21105/joss.05202

53. Lattanzi, A., Almgren, A., Quon, E., Natarajan, M., Kosovic, B., Mirocha, J., Perry, B., Wiersema, D., Wilcox, D., Yuan, X., & Zhang, W. (2025). ERF: Energy Research and Forecasting Model. *Journal of Advances in Modeling Earth Systems*, *under submission*.

54. Emes, M. J., Jafari, A., Ghanadi, F., & Arjomandi, M. (2019). Hinge and overturning moments due to unsteady heliostat pressure distributions in a turbulent atmospheric boundary layer. *Solar Energy*, *193*, 604–617. https://doi.org/10.1016/j.solener.2019.09.097